iScience

CellPress
OPEN ACCESS

Article

ADAMTS18-fibronectin interaction regulates the morphology of liver sinusoidal endothelial cells

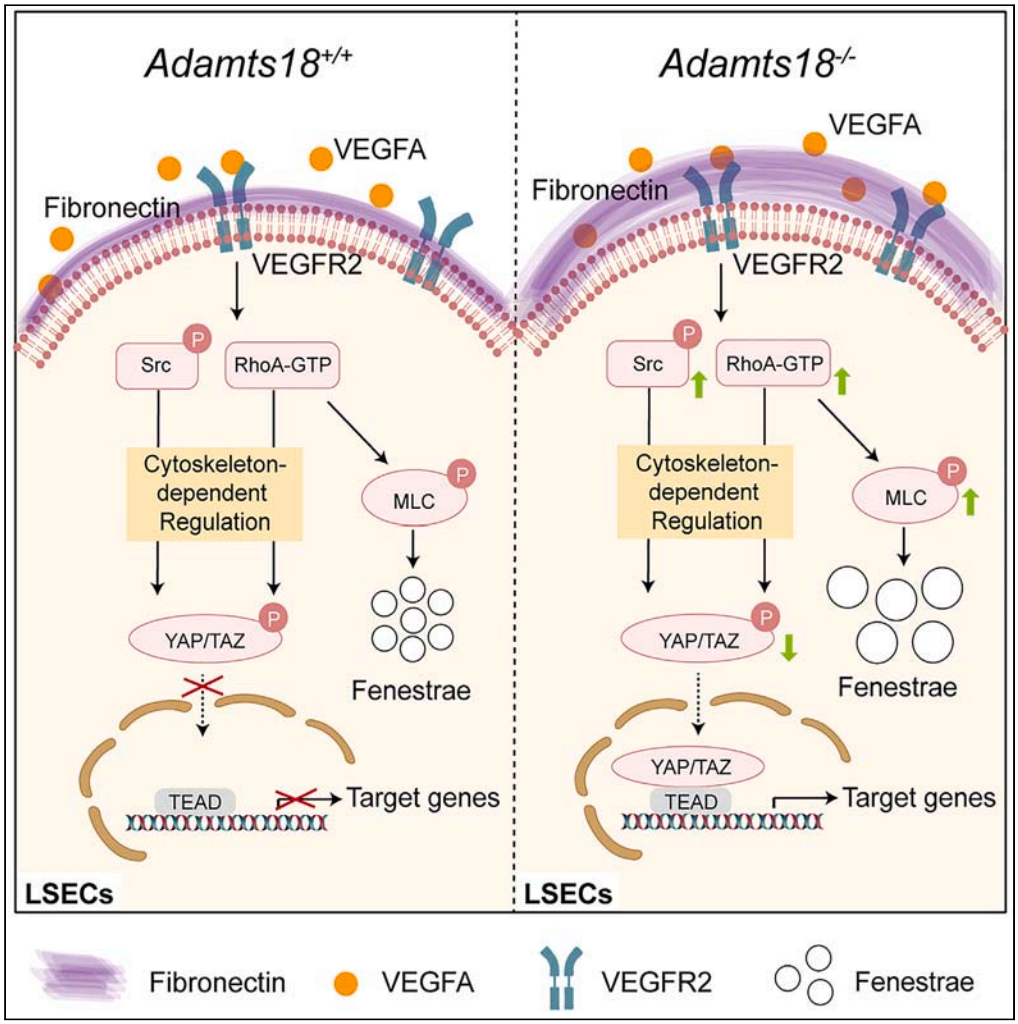

Liya Wang, Li He, Weijia Yi, ..., Yi-Hsuan Pan, Suying Dang, Wei Zhang

suyingdang@shsmu.edu.cn (S.D.)
wzhang@sat.ecnu.edu.cn (W.Z.)

Highlights

Adamts18 is expressed mainly through endothelial cells in mouse fetal liver

ADAMTS18 deficiency leads to enlarged fenestrae and increased permeability of LSECs

ADAMTS18 regulates the morphology of LSECs via affecting FN-VEGFA signaling pathway

Wang et al., iScience 27, 110273
July 19, 2024
https://doi.org/10.1016/j.isci.2024.110273

iScience

CellPress
OPEN ACCESS

Article

ADAMTS18-fibronectin interaction regulates the morphology of liver sinusoidal endothelial cells

Liya Wang,[1,3] Li He,[1,3] Weijia Yi,[1] Min Wang,[1] Fangmin Xu,[1] Hanlin Liu,[1] Jiahui Nie,[1] Yi-Hsuan Pan,[1] Suying Dang,[2,*] and Wei Zhang[1,4,*]

SUMMARY

Liver sinusoidal endothelial cells (LSECs) have a unique morphological structure known as "fenestra" that plays a crucial role in liver substance exchange and homeostasis maintenance. In this study, we demonstrate that ADAMTS18 protease is primarily secreted by fetal liver endothelial cells. ADAMTS18 deficiency leads to enlarged fenestrae and increased porosity of LSECs, microthrombus formation in liver vessels, and an imbalance of liver oxidative stress. These defects worsen carbon tetrachloride (CCl4)-induced liver fibrosis and diethylnitrosamine (DEN)/high-fat-induced hepatocellular carcinoma (HCC) in adult *Adamts18*-deficient mice. Mechanically, ADAMTS18 functions as a modifier of fibronectin (FN) to regulate the morphological acquisition of LSECs via the vascular endothelial growth factor A (VEGFA) signaling pathways. Collectively, a mechanism is proposed for LSEC morphogenesis and liver homeostasis maintenance via ADAMTS18-FN-VEGFA niches.

INTRODUCTION

Liver sinusoidal endothelial cells (LSECs) are the most permeable endothelial cells in mammals, lack basement membrane, and have a unique structure called "fenestra."[1–3] This specialized structure of LSECs acts as a dynamic filter, allowing the passage of substances such as plasma proteins, lipoproteins, drugs, and small chylomicron remnants while blood cells are retained within the sinusoids.[3,4] Thus, LSECs are the major cell type that regulate bidirectional substance transfer, protein endocytosis, immune tolerance, and sinusoidal microenvironment.[3,5–7] Recent studies have provided evidence that fenestra morphology (including diameter, porosity, and frequency) is regulated by a variety of pathophysiological conditions, such as drug metabolism, hormones, immune regulation, aging, nutritional regulation (e.g., overeating and starvation), and fibrosis.[8–10]

From an embryological perspective, LSECs originate partly from the common progenitors of endothelial and blood cells, and partly from the endocardium of venous sinus.[11,12] The development of LSECs commonly goes through three stages.[13,14] The earliest LSECs are lined with laminin-rich basement membrane, which present continuous endothelium. Then, LSECs begin to differentiate and become fenestrated; the sinusoidal matrix becomes deficient in laminin but rich in tenascin and fibronectin (FN). This differentiation process occurs around the 12th week of human gestation, and around the embryonic days (E) 14–15 of mouse embryos.[15] In this phase, formation of endothelial fenestrae is highly dependent on vascular endothelial growth factor (VEGF) signaling.[16] At birth, the size and distribution of LSECs are regionally specific, and the diameter of LSECs in portal vein region is larger than that in central region.[2,16] Extracellular matrix (ECM) components have been found to have a powerful effect on maintaining or altering the phenotype of LSECs.[17–19] However, the key factors linking ECM remodeling to LSEC morphogenesis are unknown. Addressing this question can lead to a better understanding of liver homeostasis.

ADAMTSs (a disintegrin and metalloproteinase with thrombospondin [TSP] motifs) are a family of secreted metalloproteinases with 19 members currently found in humans.[20] Through assembly and degradation of ECM molecules, such as aggrecan and proteoglycan (ADAMTS1, 4, 5, 8, 9, 15, and 20), procollagen (ADAMTS2, 3 and 14), cartilage oligomeric matrix protein (COMP) (ADAMTS7 and 12), and von Willebrand factor (vWF) (ADAMTS13), they are crucially involved in organ development and the onset and progression of many diseases.[20–23] In zebrafish and mouse models, we found that ADAMTS18 is essential for organ development and morphogenesis,[24] including several epithelial organs (e.g., lungs,[25] salivary glands,[26] and lacrimal glands[27]), vascular[28] and neuronal systems,[29] adipose tissue,[30] and reproductive tracts.[31,32] ADAMTS18 is one of the few ADAMTS family members specifically expressed in the human fetal liver.[33] However, its role in liver development is unknown. Here, we show that ADAMTS18-FN-VEGFA niche is required for the morphological acquisition of LSECs.

[1]Key Laboratory of Brain Functional Genomics (Ministry of Education and Shanghai), School of Life Sciences, East China Normal University, Shanghai, China
[2]Department of Biochemistry and Molecular Cell Biology, Shanghai Jiao Tong University School of Medicine, Shanghai, China
[3]These authors contributed equally
[4]Lead contact
*Correspondence: suyingdang@shsmu.edu.cn (S.D.), wzhang@sat.ecnu.edu.cn (W.Z.)
https://doi.org/10.1016/j.isci.2024.110273

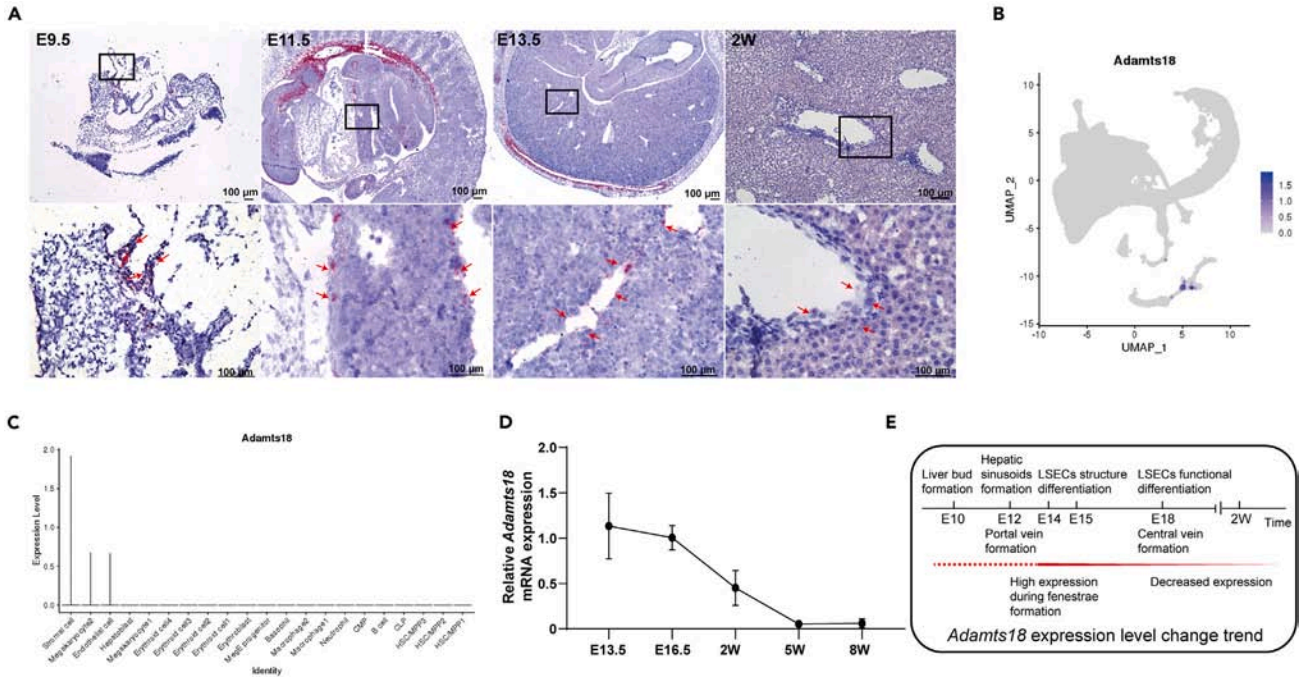

Figure 1. Spatiotemporal expression of *Adamts18* mRNA during mouse liver development

(A) ISH of wild-type embryos and liver tissues for *Adamts18*. ISH-positive signals are shown as pink dots in cells (red arrows). Scale bar, 100 μm.

(B) Uniform manifold approximation and projection (UMAP) visualization of *Adamts18* expression in cells from embryonic (E)11.5-E14.5 fetal liver.

(C) Violin plot of *Adamts18* expression levels in different cells (stromal cell, megakaryocytes, and endothelial cell). y axis indicates log-normalized expression.

(D) Real-time qPCR for *Adamts18* expression. Data are expressed as mean ± SD (n = 3/time point).

(E) Schematic representation of *Adamts18* mRNA expression levels at different stages of liver development in mice. Specifically, hepatoblasts originate from the gastrula endoderm and form liver buds at E8.5-E10. At E12, the liver bud is infiltrated by the vitelline vein, umbilical vein, and sinus venosus. Then the endothelium differentiates into the portal vein and the sinusoids. At E14–E15, LSECs become fenestrated to accommodate the hematopoietic function of the fetal liver through structural differentiation.[15] At E18, central vein formation, functional differentiation allows LSECs to adapt to the mature liver function and microenvironment.[15]

RESULTS

Spatiotemporal expression of *Adamts18* in mouse livers

To better understand the role of ADAMTS18 in liver development, the spatial and temporal expression of *Adamts18* mRNA in mouse liver tissues was assessed. *In situ* hybridization (ISH) results of E9.5 embryo whole slice showed that *Adamts18* mRNA was expressed in egg yolk and umbilical cord vessels (Figure 1A). At E11.5, *Adamts18* mRNA was mainly expressed by hepatic progenitor cells and distributed in the outer edge of liver bud. At E13.5, *Adamts18* mRNA was detected in endothelial cells of the developing liver vessels but declined rapidly at 2 weeks after birth. Using the established E11.5–E14.5 mouse fetal liver single-cell resolution cell atlas,[34] we reanalyzed the spatiotemporal expression profile of *Adamts18* via a data interactive website (http://liulab.ioz.ac.cn/fetal_liver/). The result showed that *Adamts18* was expressed in the mouse fetal liver by endothelial cells, megakaryocytes, and stromal cells (Figures 1B and 1C). The quantitative real-time PCR (real-time qPCR) data showed that *Adamts18* mRNA was mainly expressed in the embryonic stage (E13.5–16.5), and its expression was very low after 5 weeks of birth (Figure 1D). We summarized the overall trend of *Adamts18* mRNA in the liver[15] and proposed that ADAMTS18 may be associated with early vascular development in the liver (Figure 1E).

Liver development in *Adamts18*$^{-/-}$ mice

We then examined the effects of ADAMTS18 deficiency on liver development in mice. Autopsy of adult mice showed that *Adamts18*$^{-/-}$ livers had a sharper left lateral lobe margin and deeper intermediate lobe fissure and became wider laterally and shorter longitudinally than *Adamts18*$^{+/+}$ livers (Figure 2A). There was no significant difference in the ratio of liver weight to body weight between *Adamts18*$^{+/+}$ and *Adamts18*$^{-/-}$ mice (Figure 2B). At E16.5, developing monocytes with horseshoe-shaped nuclei were observed in *Adamts18*$^{-/-}$ livers (Figure 2C). At 2 weeks of age, the *Adamts18*$^{-/-}$ livers showed a significant increase in the number of Kupffer cell clumps, which were further identified by the antibody to the macrophage marker F4/80 in immunohistochemical analysis (Figures 2C, 2D, and S1A). At 2 and 9 months of age, liver histology in the liver sections stained with hematoxylin and eosin (H&E) between *Adamts18*$^{+/+}$ and *Adamts18*$^{-/-}$ mice was comparable (Figure 2C). The lobular zonation pattern of hepatocytes was comparable between the two genotypes of mice and similar to that of

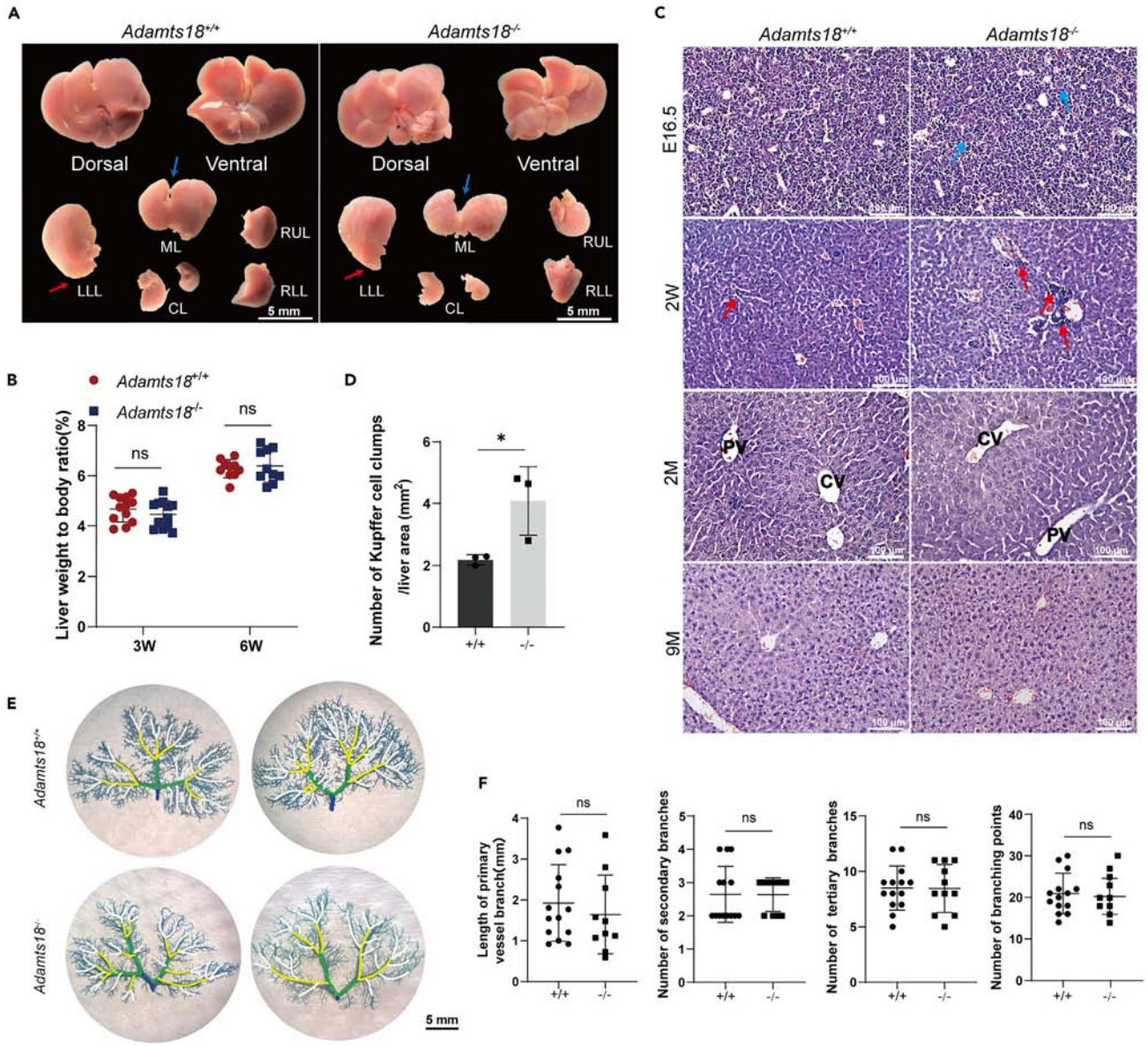

Figure 2. Effects of ADAMTS18 deficiency on liver development in mice

(A) Representative images of liver in 8-week-old adult mice. The upper parts are the dorsal and ventral views. The lower parts show the liver lobes of dorsal view. LLL, left lateral lobe; ML, middle lobe; CL, caudate lobe; RUL, right upper lobe; RLL, right lower lobe. Red arrows point out the edge of the left lateral lobe, blue arrows indicate cracks in the middle lobe. Scale bar, 5 mm.

(B) Ratio of liver weight to body weight at 3 and 6 weeks (W) of age. Data are represented as mean ± SD (n = 9∼11/time point).

(C) Hematoxylin and eosin (H&E)-stained of mouse liver sections (n = 3/time point). Blue arrows indicate monocytes. Red arrows indicate aggregated Kupffer cells. PV, portal vein; CV, central vein. Scale bar, 100 μm.

(D) Quantification of aggregated Kupffer cell clumps from liver tissues of 2-week-old mice in panel C. Data are represented as mean ± SD (n = 3).

(E) Vascular casting of the portal vein in the left lateral lobe of 8-week-old mice. Blue, green, yellow, and white marks primary, secondary, tertiary and fourth vessel, respectively. Scale bar, 5 mm.

(F) Quantification of different vascular branches and branching points in panel E by ImageJ. Data are represented as mean ± SD ($n \geq 10$). Each dot or square represents one individual. Ns, no significance; *$p < 0.05$; two-tailed Student's t test. See also Figure S1.

previous report,[35] which was evaluated by the distribution of a zonation marker E-cadherin in 2-month-old mice by immunofluorescence staining (Figure S1B). The branching of liver macrovasculature (Figures 2E and 2F) and bile duct epithelial cells (Figure S1C) were comparable between the two genotypes of mice. Basic liver function parameters, including alanine aminotransferase (ALT), aspartate aminotransferase (AST), and albumin (ALB) were comparable between the two genotypes (Figure S1D).

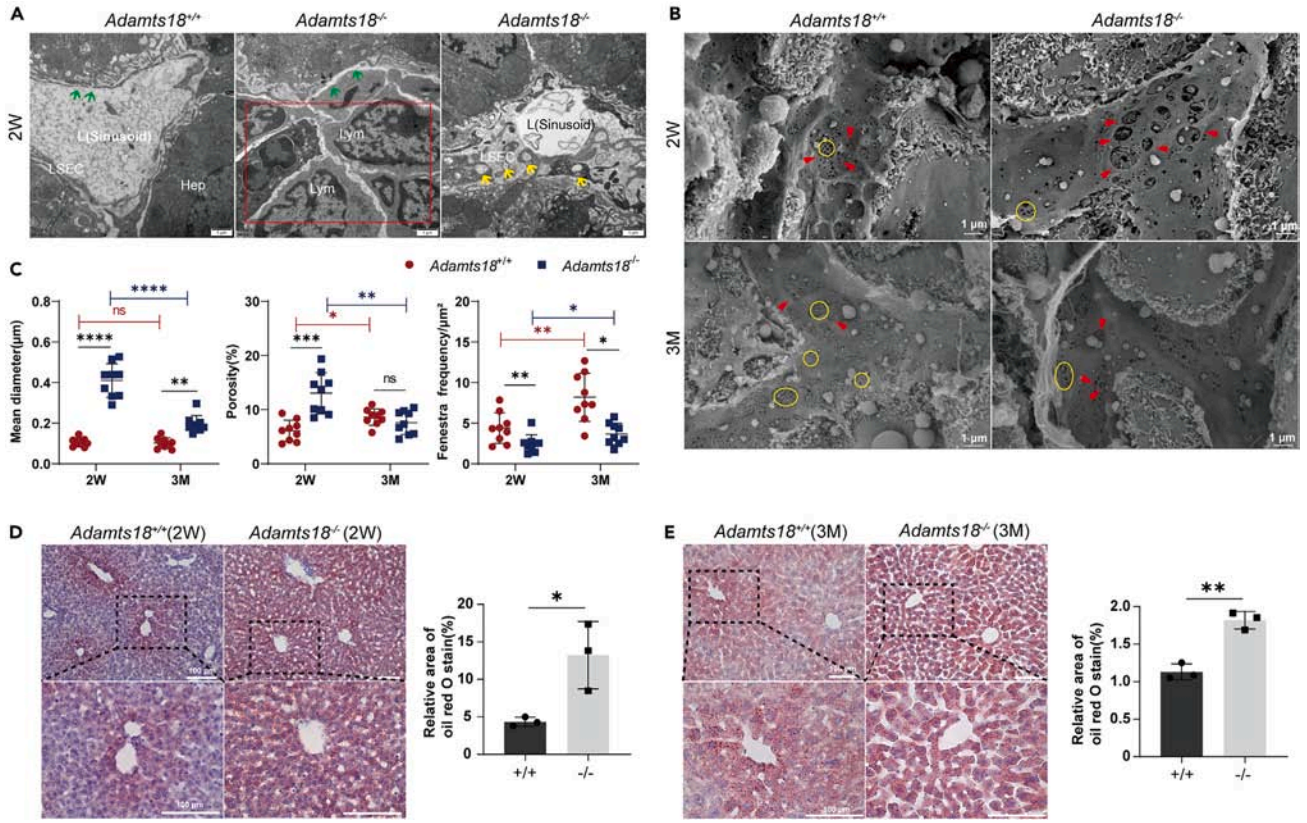

Figure 3. Enlarged LSEC fenestrae in *Adamts18*$^{-/-}$ mice

(A) TEM of LSEC morphology in 2-week-old *Adamts18*$^{+/+}$ and *Adamts18*$^{-/-}$ mice. Green arrows indicate fenestrae. Red square marks lymphocytes infiltration. Yellow arrows indicate vacuolization of hepatocytes. Hep, hepatocyte; L(Sinusoid), lumen of the sinusoid; Lym, lymphocyte. Scale bar, 1 μm.

(B) SEM of LSEC fenestrae morphology in 2-week (W)-old and 3-month (M)-old mice. Red arrows: fenestra. Yellow circles: sieve plate. Scale bar, 1 μm.

(C) Quantification of mean fenestra diameter, porosity and frequency of LSECs in panel C by ImageJ. Fenestra porosity is the percentage of the cell surface area covered by fenestra. Fenestra frequency is the number of fenestrae per area. Each dot or square represents one block. Each liver section was analyzed for 3 fields. Data are represented as mean ± SD (n = 3/time point).

(D and E) Left panel: oil red O-stained frozen mouse liver sections at 2-week (W)-old (D) and 3-month (M)-old (E). Scale bar, 100 μm. Right panel: Quantification of relative area of oil red O staining by ImageJ. Each dot or square represents one individual. Each liver section was analyzed for 5 fields. Data are represented as mean ± SD (n = 3/time point). Ns, no significance, *p < 0.05, **p < 0. 01; ***p < 0. 001; ****p < 0.0001; two-tailed Student's t test. See also Figure S2.

Enlarged LSEC fenestrae in *Adamts18*$^{-/-}$ mice

Considering that the expression peak of *Adamts18* coincides with the critical phase of fenestra formation in LSECs, we further analyzed the effect of ADAMTS18 on LSEC morphology by transmission electron microscopy (TEM) and scanning electron microscopy (SEM), respectively. The results of TEM examination showed that LSECs in 2-week-old *Adamts18*$^{-/-}$ mice contained enlarged fenestrae (Figure 3A). Meanwhile, lymphocyte infiltration and aggregation in sinusoidal lumens and hepatocyte vacuolization were observed in *Adamts18*$^{-/-}$ livers. Under SEM, the fenestra diameter and porosity of LSECs in 2-week-old *Adamts18*$^{-/-}$ mice were significantly increased (Figures 3B and 3C), suggesting increase of the permeability of liver sinusoidal cells. At 3 months of age, LSECs of *Adamts18*$^{-/-}$ mice had larger diameter and comparable porosity compared with those of *Adamts18*$^{+/+}$ mice (Figures 3B and 3C). The fenestrae gather and arrange in groups called "sieve plates."[1] The LSECs in *Adamts18*$^{+/+}$ livers were fenestrated and perforated with numerous sieve plates; while the LSECs in *Adamts18*$^{-/-}$ livers were interrupted by a number of large gaps, with a small fenestrated area, and the fenestra frequency was significantly reduced (Figure 3B). Fenestra regulates material exchange between hepatocytes and sinusoidal blood, thereby affecting lipid and glycogen metabolism.[36,37] The results of oil red O staining showed that lipid droplets in *Adamts18*$^{-/-}$ livers were accordingly increased at 2 weeks and 3 months of age (Figures 3D and 3E). The results of periodic acid Schiff (PAS) staining showed there was no significant difference in liver glycogen storage between the two genotypes of mice (Figure S2).

Impaired liver sinusoidal circulation and micro-thrombosis in *Adamts18*$^{-/-}$ mice

In addition to substance exchange, LSECs can synthesize and secrete nitric oxide, endothelin, and other active factors to regulate intrahepatic vasodilation and contraction and blood flow.[7] We therefore examined liver sinusoidal circulation under multiphoton laser scanning confocal

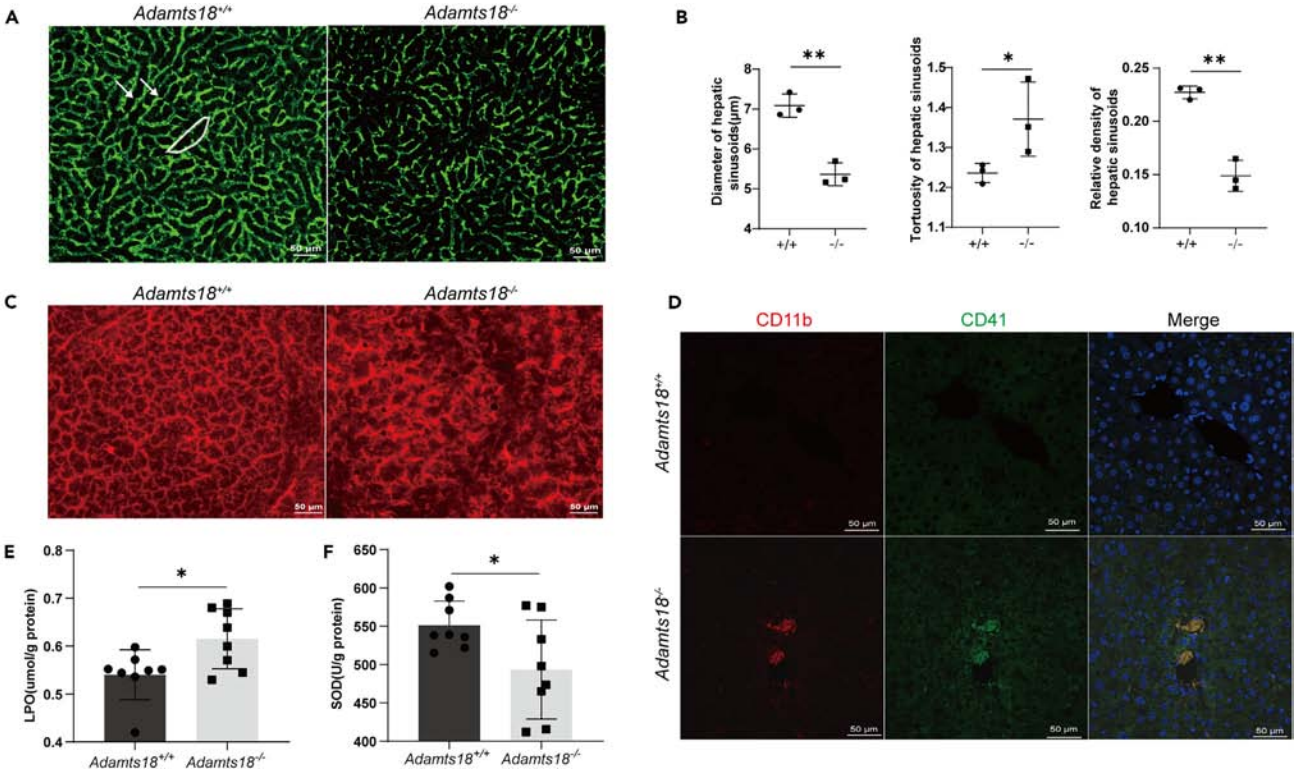

Figure 4. Tortuous liver sinusoidal circulation and liver micro-thrombosis in *Adamts18*$^{-/-}$ mice

(A) Multiphoton microscopy of liver sinusoids in 2-week-old mice. The green luminescent area represents the liver sinusoids, and the darker dots represent the red blood cells (white arrows). The ratio of the actual walking distance of the liver sinusoid to the straight walking distance is the tortuosity of the liver sinusoid (solid white lines). Scale bar, 50 μm.

(B) Quantification of diameter (left panel), tortuosity (middle panel) and relative density (right panel) of liver sinusoids in panel A by ImageJ. Data are represented as mean ± SD (n = 3).

(C) Representative images of Evans blue stained mouse liver sections at two weeks of age. Scale bar, 50 μm.

(D) Immunofluorescence of CD11b (red) and CD41 (green) in the liver vessels of 2-week-old mice, DAPI (blue). Scale bar, 50 μm.

(E and F) The level of lipid peroxidase (LPO) (E) and superoxide dismutase (SOD) (F) in the liver of 2-week-old mice determined by colorimetric method. Data are represented as mean ± SD (n = 8). Each dot or square represents one individual. Ns, no significance, *p < 0.05, **p < 0. 01; two-tailed Student's t test.

intravital microscopy. The result showed that the liver sinusoids of *Adamts18*$^{+/+}$ mice were regular and uniform, but those of *Adamts18*$^{-/-}$ mice were obviously tortuous (Figure 4A). The diameter and relative density of liver sinusoids in *Adamts18*$^{-/-}$ mice were significantly reduced, while the tortuosity was significantly increased (Figure 4B). Evans blue staining showed extravasation of the dye into the blood vessels in *Adamts18*$^{-/-}$ livers, suggesting increased LSEC permeability (Figure 4C). Remarkably, *Adamts18*$^{-/-}$ mice developed platelet-leukocyte micro-thrombi in liver vessels, shown by immunofluorescence of CD11b (a leukocyte marker) and CD41 (a platelet marker) (Figure 4D). The level of superoxide dismutase (SOD) in *Adamts18*$^{-/-}$ livers was significantly lower while the level of lipid peroxidase (LPO) was higher than that of *Adamts18*$^{+/+}$ livers (Figures 4E and 4F), indicating an imbalance of oxidative stress in *Adamts18*$^{-/-}$ livers.

Altered liver ECM compositions in *Adamts18*$^{-/-}$ livers

We then sought to elucidate the underlying mechanism by which ADAMTS18 regulates morphological acquisition of LSECs. Given ADAMTS functions as modifier of ECM proteins, we compared the changes of liver ECM compositions in 2-week-old mice. FN, laminin, and collagen types I, III, and IV are present in the early-developing perisinusoidal space.[38] By immunohistochemical staining, FN was observed to be distributed in the portal vein, central vein, and lumen of the sinusoid of both genotypes of mice, and its deposition in portal vein and lumen of liver sinusoid of *Adamts18*$^{-/-}$ mice was significantly increased (Figure 5A). Sandwich ELISA result showed that the level of total FN in liver homogenate of *Adamts18*$^{-/-}$ mice was significantly higher than that of *Adamts18*$^{+/+}$ mice (Figure 5D). FN is the first ECM molecule formed during organ development and can affect the synthesis and processing of other ECM molecules.[39,40] Immunohistochemical and Masson trichromatic staining showed comparable distribution of collagen and laminin in the portal vein region, while the levels of type III collagen and total laminin in the liver homogenate of *Adamts18*$^{-/-}$ mice were increased (Figures 5B–5D). At the transcriptional level, there was no significant difference in *Fn1* mRNA levels between the liver of the two genotypes (Figure 5E). However, the transcription expressions of *Col1a1*, *3a1*, and *Lama1* in *Adamts18*$^{-/-}$ livers were significantly up-regulated (Figure 5E). FN can affect VEGFA/VEGFR2 signaling by binding and organizing

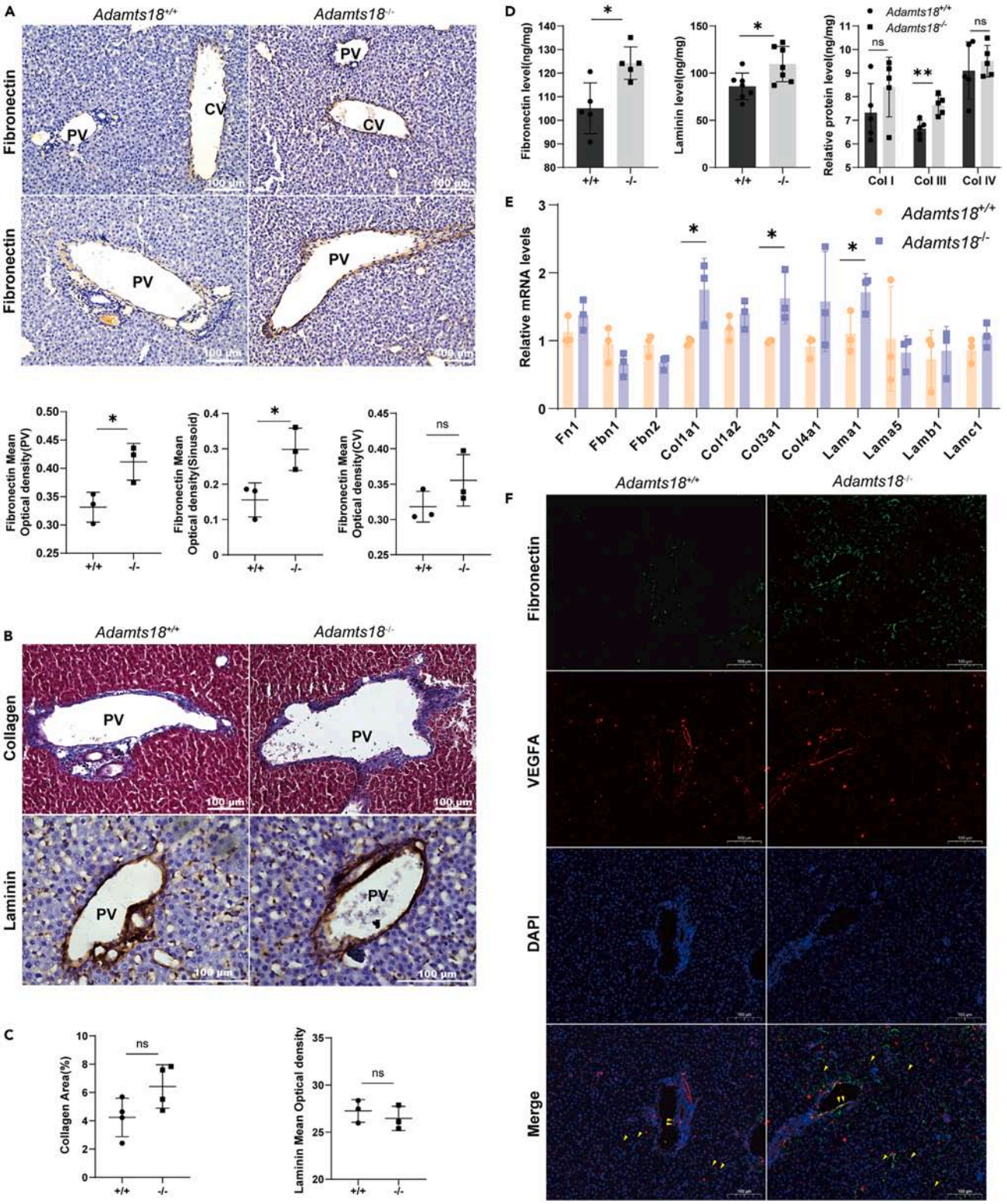
A
Adamts18+/+
Adamts18-/-
Fibronectin
PV
CV
100 μm
Fibronectin Mean Optical density(PV)
Fibronectin Mean Optical density(Sinusoid)
Fibronectin Mean Optical density(CV)
*
ns
+/+
-/-
B
Collagen
Laminin
C
Collagen Area(%)
Laminin Mean Optical density
D
Fibronectin level(ng/mg)
Laminin level(ng/mg)
Relative protein level(ng/mg)
Col I
Col III
Col IV
**
E
Relative mRNA levels
Fn1
Fbn1
Fbn2
Col1a1
Col1a2
Col3a1
Col4a1
Lama1
Lama5
Lamb1
Lamc1
F
VEGFA
DAPI
Merge

Figure 5. Altered liver ECM compositions in *Adamts18*$^{-/-}$ livers

(A) Upper panel: representative immunohistochemistry images of fibronectin (FN) in 2-week-old mouse livers. PV, portal vein; CV, central vein. Lower panel: Quantification of FN density in different hepatic vascular areas by ImageJ. Each liver section was analyzed for 5 fields. Data are represented as mean ± SD (n = 3). Scale bar, 100 μm.

(B) Upper panel: representative images of Masson's trichrome staining of collagen (Col) in 2-week-old mouse livers. Lower panel: immunohistochemistry images of Laminin in 2-week-old mouse livers. Scale bar, 100 μm.

(C) Quantification of collagen area and laminin density in panel B by ImageJ. Each liver section was analyzed for 5 fields. Data are represented as mean ± SD (n = 3).

(D) The levels of liver FN, Col I, III, IV, and laminin determined by sandwich ELISA. Data are represented as mean ± SD (n = 5∼7).

(E) Real-time qPCR results of liver ECM molecules (*Fn1*, *Fbn1*, *Fbn2*, *Col1a1*, *Col1a2*, *Col3a1*, *Col4a1*, *Lama1*, *Lama5*, *Lamb1*, and *Lamc1*). Data are represented as mean ± SD (n = 3).

(F) Representative immunofluorescence images of colocalization of FN (green) and VEGFA (red) in the liver of 2-week-old mice. Yellow arrows indicate that FN and VEGFA are co-located around blood vessels. Scale bar, 100 μm. Each dot or square represents one individual. Ns, no significance, *p < 0.05, **p < 0.01; two-tailed Student's t test.

VEGFA.[41,42] Immunofluorescence results showed that FN and VEGFA were co-localized in large vessels and peripheral liver sinusoids (Figure 5F).

Enhanced VEGFA and Rho signaling pathway in LSECs from *Adamts18*$^{-/-}$ mice

To investigate the effect of FN deposition on VEGFA signaling, we isolated primary LSECs from the liver of 2-week-old *Adamts18*$^{+/+}$ and *Adamts18*$^{-/-}$ mice and characterized the LSECs by CD14 immunofluorescence staining.[43] The results showed that high purity LSECs were obtained (Figure 6A). By Western blotting, we found VEGFA levels in *Adamts18*$^{+/+}$and *Adamts18*$^{-/-}$ LSECs were comparable, suggesting that ADAMTS18 did not directly cleave VEGFA (Figures 6B and 6C). However, VEGFA signaling pathway downstream molecules were significantly altered in *Adamts18*$^{-/-}$ LSECs. Specifically, the phosphorylation level of Src was significantly increased in *Adamts18*$^{-/-}$ LSECs (Figures 6B and 6C). Recent studies have shown that the Rho/myosin light chai (MLC) signaling pathway critically regulated the fenestra morphogenesis of LSECs and enhanced Rho/MLC activity could lead to enlarged fenestra size of LSECs.[44] The levels of active RhoA (RhoA-guanosine triphosphate [GTP]) and active MLC (pMLC) were significantly increased in *Adamts18*$^{-/-}$ LSECs (Figures 6B and 6C). VEGFA also regulates cytoskeletal changes through Src and RhoA to activate YAP/TAZ.[45] We found the phosphorylation level of YAP was significantly decreased in *Adamts18*$^{-/-}$ LSECs (Figures 6B and 6C). Immunofluorescence results were consistent with those of western blotting, with increased levels of RhoA-GTP and pMLC and decreased level of pYAP in *Adamts18*$^{-/-}$ LSECs (Figures 6D and 6E).

Interaction between ADAMTS18 and FN

Since the FN changes in liver ECM molecules were most pronounced after ADAMTS18 deletion, we sought to determine the interaction between ADAMTS18 and FN. We stably overexpressed ADAMTS18-FLAG in 293T cells and injected them into C.B17-severe combined immunodeficiency (SCID) mice to form subcutaneous tumors. Immunofluorescence results showed that ADAMTS18 and FN were co-localized in subcutaneous tumors (Figure 7A). Compared with 293T control, ADAMTS18 overexpression reduced the tissue distribution of FN.

To better understand the precise docking sites of ADAMTS18 with FN, we searched the structural fragments of ADAMTS18 and FN (Figures 7B and 7C). ADAMTS18 structure predicted by AlphaFold as receptor and protein fragments of FN as the ligands were submitted to GRAMM-X. The GRAMM-X results analyzed by PDBePISA showed the values of interface area and ΔiG (kcal/mol) (Figure 7D). GRAMM-X values of larger interface area and lower ΔiG were used to differentiate the proper models (Figure 7E). Figure S3 shows the remaining docking models generated by GRAMM-X. These predictions indicated that ADAMTS18 may bind mainly to the N-terminal fragment of FN. We further examined their interaction by co-immunoprecipitation (coIP). The results showed that N-terminal fragment of FN (81–290 aa) was pulled down by ADAMTS18 (Figure 7F).

Increased susceptibility to chemical mutagens in *Adamts18*$^{-/-}$ mice

We then sought to determine whether these developmental defects lead to spontaneous fibrosis of *Adamts18*$^{-/-}$ livers. Masson trichromatic staining showed comparable liver collagen deposition in *Adamts18*$^{+/+}$ and *Adamts18*$^{-/-}$ mice at 2 weeks, 8 weeks, and 9 months (Figures S4A and S4B), indicating that *Adamts18*$^{-/-}$ mice did not develop spontaneous liver fibrosis under normal conditions. At 2 weeks, 8 weeks, and 9 months of age, hepatic stellate cells (HSCs) determined by immunohistochemical staining of α-smooth muscle actin (α-SMA) in *Adamts18*$^{+/+}$ and *Adamts18*$^{-/-}$ livers were basically in quiescent state (Figure S4C). We then induced liver fibrosis in 8-week-old male mice with carbon tetrachloride (CCl4) challenge for 1 month (Figure 8A). Results from both Masson trichromatic staining and immunohistochemical staining of α-SMA indicated that CCl4 treatment notably increased the severity of liver fibrosis in *Adamts18*$^{-/-}$ mice (Figure 8B).

Next, we induced hepatocellular carcinoma (HCC) formation in male mice by intraperitoneal injection of diethylnitrosamine (DEN) at 2 weeks of age; mice were then given a high-fat diet at 5 weeks of age and uniformly sacrificed at 9 months of age (Figure 8C). Autopsy of mice showed that all DEN/high-fat-induced mice developed HCC and survived until 9 months of age. *Adamts18*$^{-/-}$ mice showed significant increase in liver weight/body weight ratio and the number of surface nodules (Figures 8D and 8E). Pathological analysis showed that HCC lesions were also present in the deep liver tissue, and the HCC lesions of *Adamts18*$^{-/-}$ mice were larger than those of *Adamts18*$^{+/+}$ mice (Figure 8D). In the KMplot dataset, shorter survival time/lower survival rates in human patients with liver cancer were positively correlated

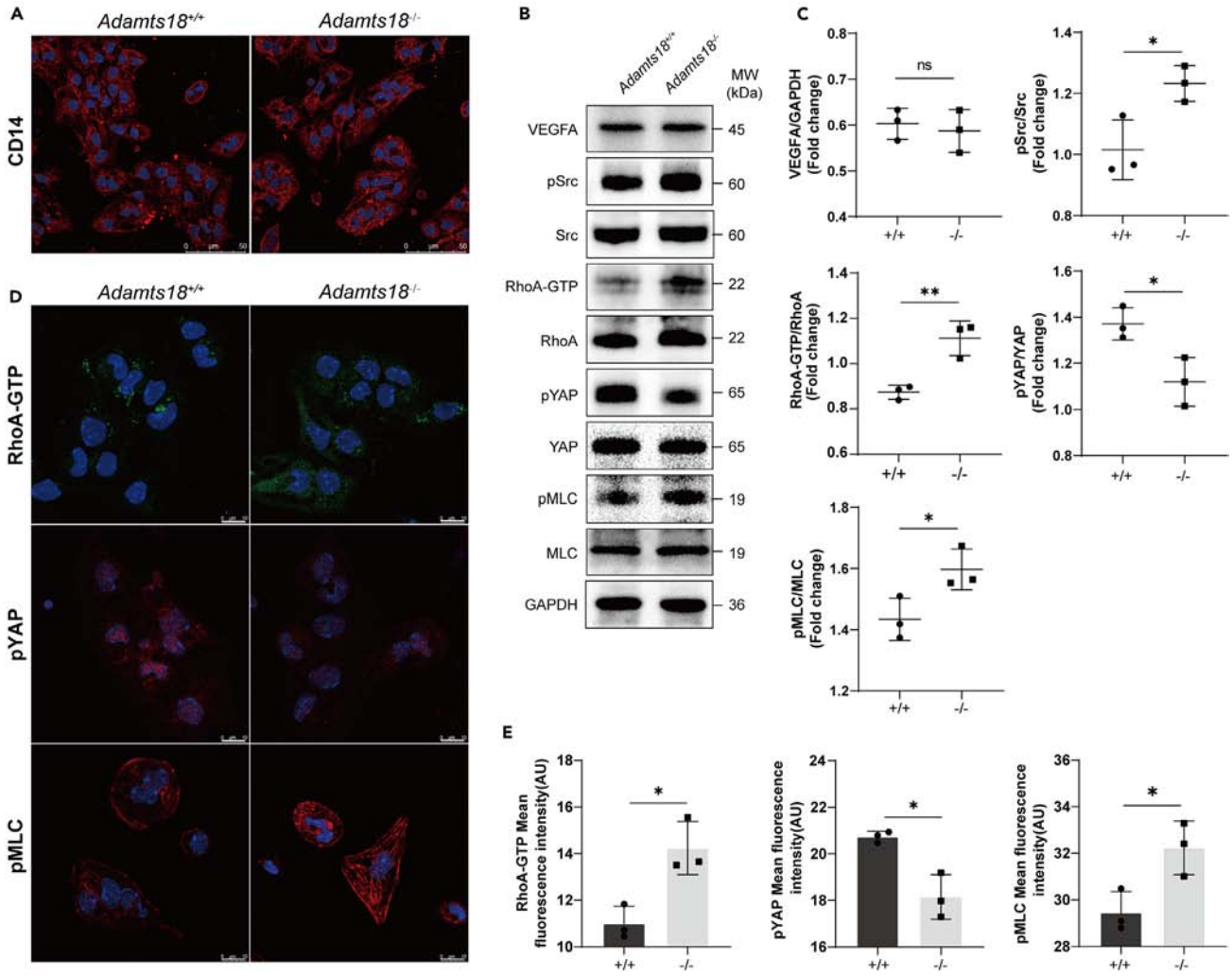

Figure 6. Enhanced VEGFA and Rho signaling pathway in LSECs from *Adamts18*$^{-/-}$ mice

(A) Immunofluorescence staining for CD14 in primary LSECs from 2-week-old *Adamts18*$^{+/+}$ and *Adamts18*$^{-/-}$ mice. Scale bar, 50 μm.

(B) Representative western blots for VEGFA, pSrc, Src, RhoA-GTP, RhoA, pYAP, YAP, pMLC, and MLC in primary LSECs.

(C) The relative quantity of VEGFA is normalized to that of GAPDH and phosphorylated proteins is normalized to that of corresponding total proteins. Data are expressed as mean ± SD (n = 3).

(D) Representative immunofluorescence staining for RhoA-GTP, pYAP, and pMLC in primary LSECs. Scale bar, 10 μm.

(E) Quantification of the fluorescence intensity in panel D by ImageJ. Each LSEC slide was analyzed for 5 fields. Data are represented as mean ± SD (n = 3). Each dot or square represents one individual. Ns, no significance, *p < 0.05, **p < 0.01; two-tailed Student's t test.

with lower *ADAMTS18* mRNA levels (Figure 8F), while the expression of other ADAMTSs, such as *ADAMTS13, 15*, and *16*, was not significantly correlated with the survival time of liver cancer patients. Overall, these results suggested that ADAMTS18 deficiency or mutations increase liver susceptibility to chemical mutagens and carcinomas.

DISCUSSION

Current knowledge about pathways regulating LSEC fenestration is still limited. In this study, we demonstrate a mechanism by which ADAMTS18 interacts with FN to regulate VEGFA signaling, which is mechanistically linked to the fenestrated morphology of LSECs.

The VEGFA signaling pathway is crucial for regulating a number of essential functions of endothelial cells, including their proliferation, migration, survival, sprouting, and permeability.[46] It has been shown that VEGFA signaling pathway promotes LSEC fenestra formation to increase cell permeability.[47,48] VEGFA bioavailability is highly regulated by ECM binding and proteolysis.[49] Studies have shown that FN is the most critical ECM molecule known to bind and organize VEGFA, determining vascular endothelial phenotype by affecting VEGFA/VEGFR2 signaling.[41,42] Stenzel et al. demonstrated that FN binds to VEGFA and regulates the downstream VEGFR2/PI3K pathway to affect

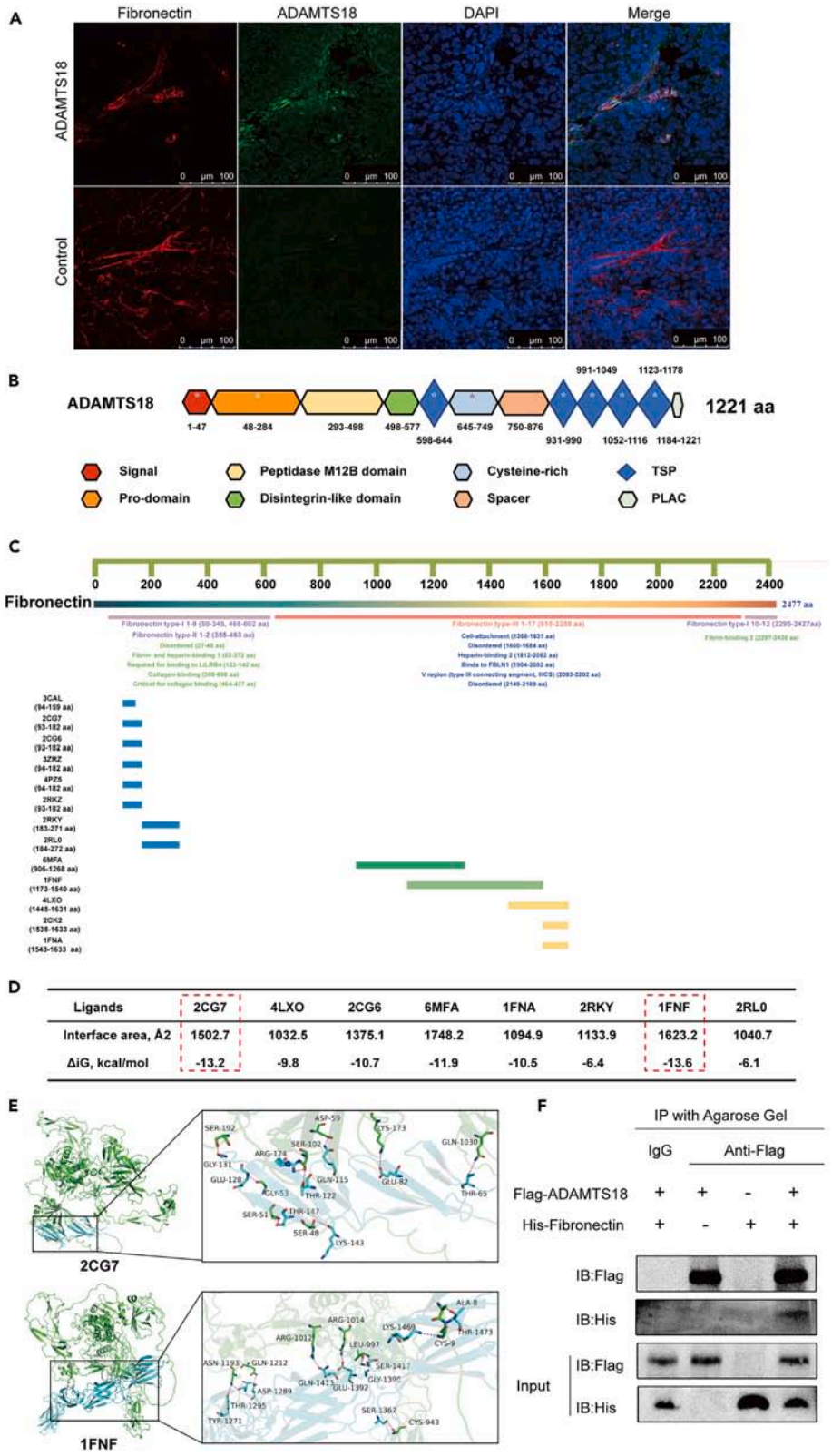

Ligands	2CG7	4LXO	2CG6	6MFA	1FNA	2RKY	1FNF	2RL0
Interface area, Å2	1502.7	1032.5	1375.1	1748.2	1094.9	1133.9	1623.2	1040.7
ΔiG, kcal/mol	-13.2	-9.8	-10.7	-11.9	-10.5	-6.4	-13.6	-6.1

Figure 7. Interaction of ADAMTS18 and FN

(A) Representative immunofluorescence images of colocalization of ADAMTS18 (green) and FN (red) in subcutaneous tumors. Scale bar, 100 μm.

(B) The basic domain organization of the ADAMTS18 and its major functional groups. * Indicates the putative region of ADAMTS18 binding FN.

(C) The location and function of 3CAL (94-159aa), 2CG7(93-182aa), 2CG6 (93–182), 3ZRZ (94-182aa), 4PZ5 (94-182aa), 2RKZ (183-271aa), 2RKY (93-182aa), 2RL0 (184-272aa), 6MFA (906-1268aa), 1FNF (1173-1540aa), 4LXO (1448-1631aa), 2CK2 (1538-1633aa), and 1FNA (1543-1633aa) in FN.

(D) The interface area and ΔiG (kcal/mol) of different protein fragments of FN and ADAMTS18 GRAMM-X docking models analyzed by PDBePISA. The red dashed boxes indicate the proper models.

(E) Two proper docking models of ADAMTS18 (green) and FN fragments (blue) generated by GRAMM-X. Interaction analysis is visualized by PyMol tool. The potential hydrogen bonding interactions (purple dashed lines) are shown in the expanded view. The upper model reveals that residues Ser48, Ser51, Ser55, Ser102, Ser192, Ser1029, Gln1030, Cys39, Gly53, and Asp59 of ADAMTS18 form hydrogen bonds with Gly144, Lys143, Thr147, Trp146, Pro126, Thr122, Gly131, Thr74, Thr65, Arg101, Glu128, and Gln115 in FN fragment (2CG7). The following model reveals that residues Arg20, Gly21, Leu22, Gly24, Gly26, Arg27, Ala31, Cys35, Lys945, His989, and Ala1022 of ADAMTS18 form hydrogen bonds with Pro87, Ser89, Leu8, Val10, Leu62, Val29, Lys86, Ala13, Thr16, Ser53, and Thr49 in FN fragment (1FNF).

(F) CoIP analysis using cellular protein extracts from HEK293T cells with co-expression and separate expression of ADAMTS18 and protein fragment of FN. Mouse immunoglobulin G (IgG) agarose gel and anti-Flag agarose gel were used for immunoprecipitation. Anti-Flag and anti-His antibody recognizing Flag-ADAMTS18, His-FN were used for immunoblotting. See also Figure S3.

retinal angiogenesis.[50] Bernier et al. found that ADAMTS18 deletion increases FN distribution to promote the VEGFA signaling pathway, thereby stimulating the fenestration of nutrient-absorbing intestinal blood vessels.[51] Through the data interactive website http://liulab.ioz.ac.cn/fetal_liver/, we found that mouse fetal liver endothelial cells could secret not only *Adamts18* but also *Vegfa* and *Fn1* (Figure S5), suggesting a possible relationship among the three molecules.[34]

In *Adamts18*$^{-/-}$ mice, we observed elevated FN accumulation around liver sinusoids as well as enlarged fenestrae, increased porosity, and permeability of LSECs. We proposed that local FN accumulation in *Adamts18*$^{-/-}$ liver alters VEGFA tissue distribution gradient, thus affecting VEGFA bioavailability, signaling pathway, and cytoskeleton. In general, VEGFA regulates cytoskeletal changes by activating Src-family kinases and RhoA/Rho kinase.[45,52,53] RhoA-GTP facilitates MLC phosphorylation via downstream Rho kinase, thereby inducing actomyosin contractility and weakening endothelial cell-cell adhesion.[54,55] MLC phosphorylation in monolayer human umbilical vein endothelial cells increases actomyosin contraction and cell permeability.[56] In LSECs, permeability is thought to be regulated by the fenestra. Studies have shown that myosin phosphorylation may be the key to regulating the diameter and number of LSEC fenestra.[8,57] Zapotoczny et al. found that MLC phosphorylation promoted actomyosin contraction at the edge of the sieve plate, leading to the increase of the fenestration diameter.[44] In the primary isolated *Adamts18*$^{-/-}$ LSECs, the downstream of VEGFA signaling pathway is significantly changed, including enhanced Src phosphorylation, RhoA activation, and MLC phosphorylation. VEGFA mediates cytoskeleton to activate YAP/TAZ, which enters the nucleus and initiates transcriptional procedures, further regulating cytoskeleton to affect permeability.[58] Wang et al. found cerebrovascular hemorrhage in YAP/TAZ endothelial-specific knockout mice, suggesting that YAP/TAZ deficiency increases endothelial cell permeability.[45] In our study, increased YAP entry into the nucleus in LSECs of *Adamts18*$^{-/-}$ mice maybe a compensatory response to increased permeability. Collectively, a mechanism is proposed for morphological acquisition of LSECs via ADAMTS18-FN-VEGFA niches.

The maximum diameter and the porosity of fenestra affect the material exchange. For example, chylomicrons exceeding the opening diameter of the fenestra cannot enter the Disse space.[1] Kazuhiko et al. revealed that, in the liver of glutamate-induced obese mice, increased accumulation of lipid droplets in hepatocytes coincided with a significant increase in the mean diameter of fenestrae.[59] In this study, we revealed that ADAMTS18 deficiency caused dysplastic LSECs with enlarged fenestrae, which may allow more and larger chylomicron remnants to enter the Disse space and hepatocytes resulting in increased lipid accumulation. On the other hand, it has been shown that hepatic lipid accumulation leads to an increase in reactive oxygen species (ROS) production,[60] which results in increased permeability through the upregulation of MLC phosphorylation and chronic inflammation.[61] We also found an imbalance of oxidative stress in *Adamts18*$^{-/-}$ liver, with inflammatory cells and platelets in liver vessels. Cogger et al. found higher doses of *tert*-butyl hydroperoxide (*t* BOOH) caused loss of sinusoidal endothelial integrity and formation of large gaps with diameters greater than 200 nm.[62] Hepatic lipid accumulation may deteriorate LSEC fenestration and function through the production ROS. We speculate that dysplastic LSEC fenestra and hepatic lipid accumulation in *Adamts18*$^{-/-}$ liver can worsen each other.

ADAMTS18 deletion resulted in increased FN deposition in the liver without *Fn1* change at the transcriptional level. In contrast, ADAMTS18 overexpression led to reduced FN distribution in subcutaneous tumors. Studies showed that soluble 70 kDa N-terminal FN is essential for assembling FN matrices through binding to linearly arranged assembly sites on the cell that are controlled by integrin α6β1-mediated adhesion.[40,63] Previously, Ataca et al. found that ADAMTS18 can cleave soluble 70 kDa N-terminal FN recombinant fragments resulting in the release of a ~30 kDa fragment *in vitro*; and the predicted cleavage site is within the I (5)-I (6) linker of FN that has been proved in its homolog ADAMTS16.[64,65] However, ADAMTS18's cleavage function requires it to have a binding region on the FN, which is unknown. Our data provided direct evidence that there exists an interaction region between ADAMTS18 and FN. Specifically, ADAMTS18 can pull down the N-terminal fragment of FN81-290; and the docking sites are associated with Gly144, Lys143, Thr147, Trp146, Pro126, Thr122, Gly131, Thr74, Thr65, Arg101, Glu128, and Gln115 in N-terminal FN. It appears that ADAMTS18 regulates FN self-assembly by cleaving N-terminal 70 kDa soluble FN fragments. However, this process is extremely complex and the detailed mechanism still needs to be further studied.

Troung et al. reported that the enlargement of the LSEC fenestra facilitates the metastasis of cancer cells to the liver.[66] Enlarged fenestrae and increased permeability of LSECs in *Adamts18*$^{-/-}$ mice may be one of the causes for the more severe HCC induced by DEN in mice. In the KMplot dataset, lower *ADAMTS18* mRNA levels were positively correlated with a poor survival in HCC patients.

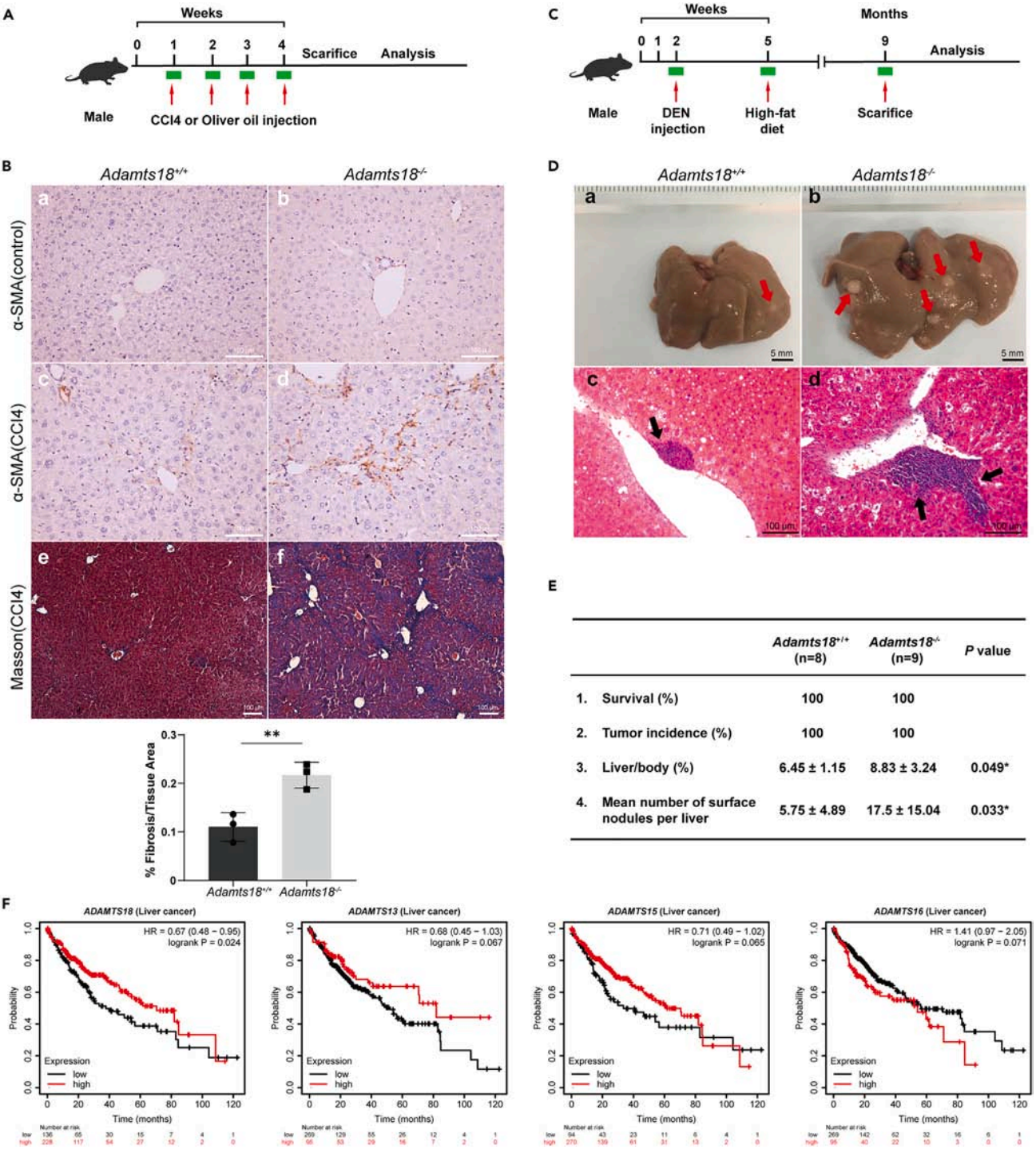

E

		Adamts18+/+ (n=8)	Adamts18-/- (n=9)	P value
1.	Survival (%)	100	100	
2.	Tumor incidence (%)	100	100	
3.	Liver/body (%)	6.45 ± 1.15	8.83 ± 3.24	0.049*
4.	Mean number of surface nodules per liver	5.75 ± 4.89	17.5 ± 15.04	0.033*

Figure 8. Increased susceptibility of *Adamts18*$^{-/-}$ mice to carbon tetrachloride (CCl4)-induced liver fibrosis and diethylnitrosamine (DEN)-induced hepatocellular carcinoma (HCC)

(A) Mode diagram of CCl4-induced liver fibrosis in 8-week-old male mice. Oliver oil acts as control.

(B) Upper panel: representative micrographs of α-smooth muscle actin (α-SMA) staining in control (a, b) and CCl4 treatment groups (c, d). Masson's trichrome staining of mouse livers with CCl4 treatment (e, f). Scale bar, 100 μm. Lower panel: quantification of fibrosis in CCl4 treatment mouse livers. Data are represented as mean ± SD (n = 3). Each dot or square represents one individual. Each liver section was analyzed for 3 fields.

(C) Induction of hepatocellular carcinoma (HCC) formation using DEN treatment in 2-week-old male mice. Mice were subsequently given high-fat diet at 5W and sacrificed at 9M.

Figure 8. *Continued*

(D) Representative images of liver in 9-month-old DEN treatment mice (a, b). Red arrows point out surface nodules. Scale bar, 5 mm. H&E-stained of mouse liver sections (c, d). Black arrows indicate nodules in the deep liver tissues. Scale bar, 100 μm.

(E) Analysis of tumor burden in DEN/high-fat-treated mice. Data are represented as mean ± SD (n = 8∼9).

(F) Correlation of *ADAMTS18*, *13*, *15*, *16* levels with the overall survival rate of human liver cancer patients in the KMplot dataset. *$p < 0.05$, **$p < 0.01$, ***$p < 0.001$; two-tailed Student's t test. See also Figure S4.

Limitations of the study

Since the sufficient amounts of purified ADAMTS18 protein are not available at present, we failed to observe whether the fenestra of LSECs can be restored after ADAMTS18 replenishment into animals *in vivo*. Nonetheless, Venkatraman et al. provide indirect evidence that TSP can induce defenestration in LSECs in a dose-dependent manner.[67] It appears that the TSP domain in ADAMTS18 has effect on the formation of fenestra structure. In addition, other soluble cytokines, such as bone morphogenetic protein 9 (BMP9) and platelet-derived growth factor B (PDGF), have also been shown to be associated with fenestra phenotype of LSECs.[68,69] We remain unclear whether these cytokines-mediated signaling pathways are also involved in the phenotypic changes of LSECs caused by ADAMTS18 deletion, which needs to be further clarified in future studies. Finally, the association between ADAMTS18 mutations and clinical congenital hepatic vascular disease is unclear and needs to be further validated in a large clinical patient sample.

STAR★METHODS

Detailed methods are provided in the online version of this paper and include the following:

- KEY RESOURCES TABLE
- RESOURCE AVAILABILITY
  - Lead contact
  - Materials availability
  - Data and code availability
- EXPERIMENTAL MODEL AND STUDY PARTICIPANT DETAILS
  - Animals
  - Carbon tetrachloride (CCl4) induced liver fibrosis model
  - Diethylnitrosamine (DEN) induced hepatocellular carcinoma (HCC) model
- METHOD DETAILS
  - Materials
  - RNA *in situ* hybridization, qRT-PCR, Histology, immunohistochemistry, and immunofluorescence
  - Blood vessel cast
  - Electron microscopy
  - Multiphoton laser scanning confocal intravital microscopy (IVM)
  - Enzyme linked immunosorbent assay
  - Assay of liver vascular permeability
  - LSECs isolation
  - Cell immunofluorescence
  - RhoA activity
  - Cell culture and co-localization assay
  - Protein–protein docking study
  - Co-immunoprecipitation (IP)
- QUANTIFICATION AND STATISTICAL ANALYSIS

SUPPLEMENTAL INFORMATION

Supplemental information can be found online at https://doi.org/10.1016/j.isci.2024.110273.

ACKNOWLEDGMENTS

The authors thank the Core Facility of Basic Medical Science, Shanghai Jiao Tong University School of Medicine, for technical support of electron microscopy analysis. This work was supported by grants from the National Natural Science Foundation of China (81170481) and Shanghai Municipal Natural Science Foundation (16ZR1423700).

AUTHOR CONTRIBUTIONS

W.Z. and S.D. were involved in the research design. All authors were involved in the research implementation and data analyses. W.Z., S.D., L.W., and L.H. wrote the paper.

DECLARATION OF INTERESTS

The authors declare no competing interests.

Received: December 29, 2023
Revised: May 12, 2024
Accepted: June 12, 2024
Published: June 14, 2024

REFERENCES

1. Wisse, E., De Zanger, R.B., Charels, K., Van Der Smissen, P., and McCuskey, R.S. (1985). The liver sieve: considerations concerning the structure and function of endothelial fenestrae, the sinusoidal wall and the space of Disse. Hepatology *5*, 683–692. https://doi.org/10.1002/hep.1840050427.
2. Couvelard, A., Scoazec, J.-Y., Dauge, M.-C., Bringuier, A.-F., Potet, F., and Feldmann, G. (1996). Structural and Functional Differentiation of Sinusoidal Endothelial Cells During Liver Organogenesis in Humans. Blood *87*, 4568–4580. https://doi.org/10.1182/blood.V87.11.4568.bloodjournal87114568.
3. Sørensen, K.K., Simon-Santamaria, J., McCuskey, R.S., and Smedsrød, B. (2015). Liver Sinusoidal Endothelial Cells. Compr. Physiol. *5*, 1751–1774. https://doi.org/10.1002/cphy.c140078.
4. Ben-Moshe, S., and Itzkovitz, S. (2019). Spatial heterogeneity in the mammalian liver. Nat. Rev. Gastro. Hepat. *16*, 395–410. https://doi.org/10.1038/s41575-019-0134-x.
5. Sørensen, K.K., McCourt, P., Berg, T., Crossley, C., Le Couteur, D., Wake, K., and Smedsrød, B. (2012). The scavenger endothelial cell: a new player in homeostasis and immunity. Am. J. Physiol. Regul. Integr. Comp. Physiol. *303*, R1217–R1230. https://doi.org/10.1152/ajpregu.00686.2011.
6. DeLeve, L.D., and Maretti-Mira, A.C. (2017). Liver Sinusoidal Endothelial Cell: An Update. Semin. Liver Dis. *37*, 377–387. https://doi.org/10.1055/s-0037-1617455.
7. Poisson, J., Lemoinne, S., Boulanger, C., Durand, F., Moreau, R., Valla, D., and Rautou, P.-E. (2017). Liver sinusoidal endothelial cells: Physiology and role in liver diseases. J. Hepatol. *66*, 212–227. https://doi.org/10.1016/j.jhep.2016.07.009.
8. Szafranska, K., Kruse, L.D., Holte, C.F., McCourt, P., and Zapotoczny, B. (2021). The wHole Story About Fenestrations in LSEC. Front. Physiol. *12*, 735573. https://doi.org/10.3389/fphys.2021.735573.
9. DeLeve, L.D. (2015). Liver sinusoidal endothelial cells in hepatic fibrosis. Hepatology *61*, 1740–1746. https://doi.org/10.1002/hep.27376.
10. Grosse, L., and Bulavin, D.V. (2020). LSEC model of aging. Aging (milano) *12*, 11152–11160. https://doi.org/10.18632/aging.103492.
11. Collardeau-Frachon, S., and Scoazec, J.-Y. (2008). Vascular development and differentiation during human liver organogenesis. Anat. Rec. *291*, 614–627. https://doi.org/10.1002/ar.20679.
12. Lotto, J., Stephan, T.L., and Hoodless, P.A. (2023). Fetal liver development and implications for liver disease pathogenesis. Nat. Rev. Gastroenterol. Hepatol. *20*, 561–581. https://doi.org/10.1038/s41575-023-00775-2.
13. Gouysse, G., Couvelard, A., Frachon, S., Bouvier, R., Nejjari, M., Dauge, M.C., Feldmann, G., Hénin, D., and Scoazec, J.Y. (2002). Relationship between vascular development and vascular differentiation during liver organogenesis in humans. J. Hepatol. *37*, 730–740. https://doi.org/10.1016/s0168-8278(02)00282-9.
14. Liang, Y., Kaneko, K., Xin, B., Lee, J., Sun, X., Zhang, K., and Feng, G.-S. (2022). Temporal analyses of postnatal liver development and maturation by single-cell transcriptomics. Dev. Cell *57*, 398–414.e5. https://doi.org/10.1016/j.devcel.2022.01.004.
15. Gómez-Salinero, J.M., Izzo, F., Lin, Y., Houghton, S., Itkin, T., Geng, F., Bram, Y., Adelson, R.P., Lu, T.M., Inghirami, G., et al. (2022). Specification of fetal liver endothelial progenitors to functional zonated adult sinusoids requires c-Maf induction. Cell Stem Cell *29*, 593–609.e7. https://doi.org/10.1016/j.stem.2022.03.002.
16. Ober, E.A., and Lemaigre, F.P. (2018). Development of the liver: Insights into organ and tissue morphogenesis. J. Hepatol. *68*, 1049–1062. https://doi.org/10.1016/j.jhep.2018.01.005.
17. Brougham-Cook, A., Kimmel, H.R.C., Monckton, C.P., Owen, D., Khetani, S.R., and Underhill, G.H. (2022). Engineered matrix microenvironments reveal the heterogeneity of liver sinusoidal endothelial cell phenotypic responses. APL Bioeng. *6*, 046102. https://doi.org/10.1063/5.0097602.
18. Sellaro, T.L., Ravindra, A.K., Stolz, D.B., and Badylak, S.F. (2007). Maintenance of hepatic sinusoidal endothelial cell phenotype in vitro using organ-specific extracellular matrix scaffolds. Tissue Eng. *13*, 2301–2310. https://doi.org/10.1089/ten.2006.0437.
19. McGuire, R.F., Bissell, D.M., Boyles, J., and Roll, F.J. (1992). Role of extracellular matrix in regulating fenestrations of sinusoidal endothelial cells isolated from normal rat liver. Hepatology *15*, 989–997. https://doi.org/10.1002/hep.1840150603.
20. Kelwick, R., Desanlis, I., Wheeler, G.N., and Edwards, D.R. (2015). The ADAMTS (A Disintegrin and Metalloproteinase with Thrombospondin motifs) family. Genome Biol. *16*, 113. https://doi.org/10.1186/s13059-015-0676-3.
21. Gibson, S.V., Madzharova, E., Tan, A.C., Allen, M.D., Keller, U.A.d., Louise Jones, J., Carter, E.P., and Grose, R.P. (2023). ADAMTS3 restricts cancer invasion in models of early breast cancer progression through enhanced fibronectin degradation. Matrix Biol. *121*, 74–89. https://doi.org/10.1016/j.matbio.2023.06.005.
22. Mead, T.J., and Apte, S.S. (2018). ADAMTS proteins in human disorders. Matrix Biol. *71–72*, 225–239. https://doi.org/10.1016/j.matbio.2018.06.002.
23. Iruela-Arispe, M.L., Carpizo, D., and Luque, A. (2003). ADAMTS1: a matrix metalloprotease with angioinhibitory properties. Sci. *995*, 183–190. https://doi.org/10.1111/j.1749-6632.2003.tb03221.x.
24. Lu, T., Zhang, T., Wang, C., Yang, N., Pan, Y.H., Dang, S., and Zhang, W. (2020). Adamts18 deficiency in zebrafish embryo causes defective trunk angiogenesis and caudal vein plexus formation. Biochem. Biophys. Res. Commun. *521*, 907–913. https://doi.org/10.1016/j.bbrc.2019.10.202.
25. Lu, T., Lin, X., Pan, Y.-H., Yang, N., Ye, S., Zhang, Q., Wang, C., Zhu, R., Zhang, T., Wisniewski, T.M., et al. (2020). ADAMTS18 Deficiency Leads to Pulmonary Hypoplasia and Bronchial Microfibril Accumulation. iScience *23*, 101472. https://doi.org/10.1016/j.isci.2020.101472.
26. Yang, N., Zhang, Q., Ye, S., Lu, T., Sun, M., Wang, L., Wang, M., Pan, Y.H., Dang, S., and Zhang, W. (2022). Adamts18 Deficiency Causes Spontaneous SMG Fibrogenesis in Adult Mice. J. Dent. Res. *101*, 226–234. https://doi.org/10.1177/00220345211029270.
27. Wang, L., Sun, M., Zhang, Q., Dang, S., and Zhang, W. (2022). ADAMTS18 regulates early branching morphogenesis of lacrimal gland and has a significant association with the risk of dry eye in mice. Exp. Eye Res. *218*, 109020. https://doi.org/10.1016/j.exer.2022.109020.
28. Ye, S., Yang, N., Lu, T., Wu, T., Wang, L., Pan, Y.-H., Cao, X., Yuan, X., Wisniewski, T., Dang, S., and Zhang, W. (2021). Adamts18 modulates the development of the aortic arch and common carotid artery. iScience *24*, 102672. https://doi.org/10.1016/j.isci.2021.102672.
29. Zhu, R., Pan, Y.-H., Sun, L., Zhang, T., Wang, C., Ye, S., Yang, N., Lu, T., Wisniewski, T., Dang, S., and Zhang, W. (2019). ADAMTS18 Deficiency Affects Neuronal Morphogenesis and Reduces the Levels of Depression-like Behaviors in Mice. Neuroscience *399*, 53–64. https://doi.org/10.1016/j.neuroscience.2018.12.025.
30. Zhu, R., Cheng, M., Lu, T., Yang, N., Ye, S., Pan, Y.-H., Hong, T., Dang, S., and Zhang, W. (2018). A Disintegrin and Metalloproteinase with Thrombospondin Motifs 18 Deficiency Leads to Visceral Adiposity and Associated Metabolic Syndrome in Mice. Am. J. Pathol. *188*, 461–473. https://doi.org/10.1016/j.ajpath.2017.10.020.
31. Lin, X., Wu, T., Wang, L., Dang, S., and Zhang, W. (2021). ADAMTS18 deficiency leads to preputial gland hypoplasia and fibrosis in male mice. Reprod. Biol. *21*, 100542. https://doi.org/10.1016/j.repbio.2021.100542.
32. Lin, X., Wang, C., Zhang, Q., Pan, Y.-H., Dang, S., and Zhang, W. (2021). ADAMTS18 regulates vaginal opening through influencing the fusion of Mullerian duct and apoptosis of vaginal epithelial cells in mice.

Reprod. Biol. *21*, 100537. https://doi.org/10.1016/j.repbio.2021.100537.
33. Cal, S., Obaya, A.J., Llamazares, M., Garabaya, C., Quesada, V., and López-Otín, C. (2002). Cloning, expression analysis, and structural characterization of seven novel human ADAMTSs, a family of metalloproteinases with disintegrin and thrombospondin-1 domains. Gene *283*, 49–62. https://doi.org/10.1016/S0378-1119(01)00861-7.
34. Gao, S., Shi, Q., Zhang, Y., Liang, G., Kang, Z., Huang, B., Ma, D., Wang, L., Jiao, J., Fang, X., et al. (2022). Identification of HSC/MPP expansion units in fetal liver by single-cell spatiotemporal transcriptomics. Cell Res. *32*, 38–53. https://doi.org/10.1038/s41422-021-00540-7.
35. Ben-Moshe, S., Shapira, Y., Moor, A.E., Manco, R., Veg, T., Bahar Halpern, K., and Itzkovitz, S. (2019). Spatial sorting enables comprehensive characterization of liver zonation. Nat. Metab. *1*, 899–911. https://doi.org/10.1038/s42255-019-0109-9.
36. Zuo, B., Yang, F., Huang, L., Han, J., Li, T., Ma, Z., Cao, L., Li, Y., Bai, X., Jiang, M., et al. (2024). Endothelial Slc35a1 deficiency causes loss of LSEC identity and exacerbates neonatal lipid deposition in the liver in mice. Cell. Mol. Gastroenterol. Hepatol. *17*, 1039–1061. https://doi.org/10.1016/j.jcmgh.2024.03.002.
37. Wei, Z., Lei, J., Shen, F., Dai, Y., Sun, Y., Liu, Y., Dai, Y., Jian, Z., Wang, S., Chen, Z., et al. (2020). Cavin1 Deficiency Causes Disorder of Hepatic Glycogen Metabolism and Neonatal Death by Impacting Fenestrations in Liver Sinusoidal Endothelial Cells. Adv. Sci. *7*, 2000963. https://doi.org/10.1002/advs.202000963.
38. Amenta, P.S., and Harrison, D. (1997). Expression and potential role of the extracellular matrix in hepatic ontogenesis: a review. Microsc. Res. Tech. *39*, 372–386. https://doi.org/10.1002/(SICI)1097-0029(19971115)39:4<372::AID-JEMT7>3.0.CO;2-J.
39. Patten, J., and Wang, K. (2021). Fibronectin in development and wound healing. Adv. Drug Deliv. Rev. *170*, 353–368. https://doi.org/10.1016/j.addr.2020.09.005.
40. Dalton, C.J., and Lemmon, C.A. (2021). Fibronectin: Molecular structure, fibrillar structure and mechanochemical signaling. Cells *10*, 2443. https://doi.org/10.3390/cells10092443.
41. Wijelath, E.S., Rahman, S., Murray, J., Patel, Y., Savidge, G., and Sobel, M. (2004). Fibronectin promotes VEGF-induced CD34 cell differentiation into endothelial cells. J. Vasc. Surg. *39*, 655–660. https://doi.org/10.1016/j.jvs.2003.10.042.
42. Usuelli, M., Meyer, T., Mezzenga, R., and Mitsi, M. (2021). VEGF and VEGFR2 bind to similar pH-sensitive sites on fibronectin, exposed by heparin-mediated conformational changes. J. Biol. Chem. *296*, 100584. https://doi.org/10.1016/j.jbc.2021.100584.
43. Meyer, J., Gonelle-Gispert, C., Morel, P., and Bühler, L. (2016). Methods for Isolation and Purification of Murine Liver Sinusoidal Endothelial Cells: A Systematic Review. PLoS One *11*, e0151945. https://doi.org/10.1371/journal.pone.0151945.
44. Zapotoczny, B., Szafranska, K., Lekka, M., Ahluwalia, B.S., and McCourt, P. (2022). Tuning of Liver Sieve: The Interplay between Actin and Myosin Regulatory Light Chain Regulates Fenestration Size and Number in Murine Liver Sinusoidal Endothelial Cells. Int. J. Mol. Sci. *23*, 9850. https://doi.org/10.3390/ijms23179850.
45. Wang, X., Freire Valls, A., Schermann, G., Shen, Y., Moya, I.M., Castro, L., Urban, S., Solecki, G.M., Winkler, F., Riedemann, L., et al. (2017). YAP/TAZ Orchestrate VEGF Signaling during Developmental Angiogenesis. Dev. Cell *42*, 462–478.e7. https://doi.org/10.1016/j.devcel.2017.08.002.
46. Apte, R.S., Chen, D.S., and Ferrara, N. (2019). VEGF in signaling and disease: Beyond discovery and development. Cell *176*, 1248–1264. https://doi.org/10.1016/j.cell.2019.01.021.
47. Funyu, J., Mochida, S., Inao, M., Matsui, A., and Fujiwara, K. (2001). VEGF can act as vascular permeability factor in the hepatic sinusoids through upregulation of porosity of endothelial cells. Biochem. Biophys. Res. Commun. *280*, 481–485. https://doi.org/10.1006/bbrc.2000.4148.
48. Yokomori, H., Oda, M., Yoshimura, K., Nagai, T., Ogi, M., Nomura, M., and Ishii, H. (2003). Vascular endothelial growth factor increases fenestral permeability in hepatic sinusoidal endothelial cells. Liver Int. *23*, 467–475. https://doi.org/10.1111/j.1478-3231.2003.00880.x.
49. Ferrara, N. (2010). Binding to the extracellular matrix and proteolytic processing: Two key mechanisms regulating vascular endothelial growth factor action. Mol. Biol. Cell *21*, 687–690. https://doi.org/10.1091/mbc.e09-07-0590.
50. Stenzel, D., Lundkvist, A., Sauvaget, D., Busse, M., Graupera, M., van der Flier, A., Wijelath, E.S., Murray, J., Sobel, M., Costell, M., et al. (2011). Integrin-dependent and -independent functions of astrocytic fibronectin in retinal angiogenesis. Development (Cambridge, England) *138*, 4451–4463. https://doi.org/10.1242/dev.071381.
51. Bernier-Latmani, J., Mauri, C., Marcone, R., Renevey, F., Durot, S., He, L., Vanlandewijck, M., Maclachlan, C., Davanture, S., Zamboni, N., et al. (2022). ADAMTS18+ villus tip telocytes maintain a polarized VEGFA signaling domain and fenestrations in nutrient-absorbing intestinal blood vessels. Nat. Commun. *13*, 3983. https://doi.org/10.1038/s41467-022-31571-2.
52. van Nieuw Amerongen, G.P., Koolwijk, P., Versteilen, A., and van Hinsbergh, V.W.M. (2003). Involvement of RhoA/Rho kinase signaling in VEGF-induced endothelial cell migration and angiogenesis in vitro. Arterioscler. Thromb. Vasc. Biol. *23*, 211–217. https://doi.org/10.1161/01.atv.0000054198.68894.88.
53. Sun, Z., Li, X., Massena, S., Kutschera, S., Padhan, N., Gualandi, L., Sundvold-Gjerstad, V., Gustafsson, K., Choy, W.W., Zang, G., et al. (2012). VEGFR2 induces c-src signaling and vascular permeability in vivo via the adaptor protein TSAd. J. Exp. Med. *209*, 1363–1377. https://doi.org/10.1084/jem.20111343.
54. Shen, Q., Rigor, R.R., Pivetti, C.D., Wu, M.H., and Yuan, S.Y. (2010). Myosin light chain kinase in microvascular endothelial barrier function. Cardiovasc. Res. *87*, 272–280. https://doi.org/10.1093/cvr/cvq144.
55. Han, J.y., Yi, Y., Liang, A.h., Zhang, Y.-S., Li, C.y., Wang, L.m., Pan, C., and Zhao, Y. (2016). Research progress of rho/ROCK signal pathway. Yao xue xue bao = Acta pharmaceutica Sinica *51*, 853–859. https://doi.org/10.16438/j.0513-4870.2015-0906.
56. Shen, Q., Rigor, R.R., Pivetti, C.D., Wu, M.H., and Yuan, S.Y. (2010). Myosin light chain kinase in microvascular endothelial barrier function. Cardiovasc. Res. *87*, 272–280. https://doi.org/10.1093/cvr/cvq144.
57. Yokomori, H., Yoshimura, K., Nagai, T., Fujimaki, K., Nomura, M., Hibi, T., Ishii, H., and Oda, M. (2004). Sinusoidal endothelial fenestrae organization regulated by myosin light chain kinase and Rho-kinase in cultured rat sinusoidal endothelial cells. Hepatol. Res. *30*, 169–174. https://doi.org/10.1016/j.hepres.2004.08.002.
58. Ritsvall, O., and Albinsson, S. (2024). Emerging role of YAP/TAZ in vascular mechanotransduction and disease. Microcirculation *31*, e12838. https://doi.org/10.1111/micc.12838.
59. Kazuhiko, N.,K.M., and S, T.-N. (2015). Dilatation of sinusoidal capillary and swelling of sinusoidal fenestration in obesity: an ultrastructural study. Ultrastruct. Pathol. *39*, 30–37. https://doi.org/10.3109/01913123.2014.947010.
60. Chen, Z., Tian, R., She, Z., Cai, J., and Li, H. (2020). Role of oxidative stress in the pathogenesis of nonalcoholic fatty liver disease. Free Radic. Biol. Med. *152*, 116–141. https://doi.org/10.1016/j.freeradbiomed.2020.02.025.
61. Lum, H., and Roebuck, K.A. (2001). Oxidant stress and endothelial cell dysfunction. Am. J. Physiol. Cell Physiol. *280*, C719–C741. https://doi.org/10.1152/ajpcell.2001.280.4.C719.
62. Cogger, V.C., Muller, M., Fraser, R., McLean, A.J., Khan, J., and Le Couteur, D.G. (2004). The effects of oxidative stress on the liver sieve. J. Hepatol. *41*, 370–376. https://doi.org/10.1016/j.jhep.2004.04.034.
63. Tomasini-Johansson, B.R., Annis, D.S., and Mosher, D.F. (2006). The N-terminal 70-kDa fragment of fibronectin binds to cell surface fibronectin assembly sites in the absence of intact fibronectin. Matrix Biol. *25*, 282–293. https://doi.org/10.1016/j.matbio.2006.02.002.
64. Ataca, D., Aouad, P., Constantin, C., Laszlo, C., Beleut, M., Shamseddin, M., Rajaram, R.D., Jeitziner, R., Mead, T.J., Caikovski, M., et al. (2020). The secreted protease Adamts18 links hormone action to activation of the mammary stem cell niche. Nat. Commun. *11*, 1571. https://doi.org/10.1038/s41467-020-15357-y.
65. Schnellmann, R., Sack, R., Hess, D., Annis, D.S., Mosher, D.F., Apte, S.S., and Chiquet-Ehrismann, R. (2018). A Selective Extracellular Matrix Proteomics Approach Identifies Fibronectin Proteolysis by A Disintegrin-like and Metalloprotease Domain with Thrombospondin Type 1 Motifs (ADAMTS16) and Its Impact on Spheroid Morphogenesis. Mol. Cell. Proteomics *17*, 1410–1425. https://doi.org/10.1074/mcp.RA118.000676.
66. Huu Hoang, T., Sato-Matsubara, M., Yuasa, H., Matsubara, T., Thuy, L.T.T., Ikenaga, H., Phuong, D.M., Hanh, N.V., Hieu, V.N., Hoang, D.V., et al. (2022). Cancer cells produce liver metastasis via gap formation in sinusoidal endothelial cells through proinflammatory paracrine mechanisms. Sci. Adv. *8*, eabo5525. https://doi.org/10.1126/sciadv.abo5525.
67. Venkatraman, L., and Tucker-Kellogg, L. (2013). The CD47-binding peptide of thrombospondin-1 induces defenestration of liver sinusoidal endothelial cells. Liver Int. *33*, 1386–1397. https://doi.org/10.1111/liv.12231.

68. Desroches-Castan, A., Tillet, E., Ricard, N., Ouarné, M., Mallet, C., Belmudes, L., Couté, Y., Boillot, O., Scoazec, J.-Y., Bailly, S., and Feige, J.J. (2019). Bone Morphogenetic Protein 9 Is a Paracrine Factor Controlling Liver Sinusoidal Endothelial Cell Fenestration and Protecting Against Hepatic Fibrosis. Hepatology *70*, 1392–1408. https://doi.org/10.1002/hep.30655.

69. Raines, S.M., Richards, O.C., Schneider, L.R., Schueler, K.L., Rabaglia, M.E., Oler, A.T., Stapleton, D.S., Genové, G., Dawson, J.A., Betsholtz, C., and Attie, A.D. (2011). Loss of PDGF-B activity increases hepatic vascular permeability and enhances insulin sensitivity. Am. J. Physiol. Endocrinol. Metab. *301*, E517–E526. https://doi.org/10.1152/ajpendo.00241.2011.

70. Lu, T., Dang, S., Zhu, R., Wang, Y., Nie, Z., Hong, T., and Zhang, W. (2017). Adamts18 deficiency promotes colon carcinogenesis by enhancing β-catenin and p38MAPK/ERK1/2 signaling in the mouse model of AOM/DSS-induced colitis-associated colorectal cancer. Oncotarget *8*, 18979–18990. https://doi.org/10.18632/oncotarget.14866.

71. Radu, M., and Chernoff, J. (2013). An in vivo assay to test blood vessel permeability. J. Vis. Exp. e50062. https://doi.org/10.3791/50062.

72. Guo, Q., Furuta, K., Aly, A., and Ibrahim, S.H. (2021). Isolation and Characterization of Mouse Primary Liver Sinusoidal Endothelial Cells. J. Vis. Exp. https://doi.org/10.3791/63062.

73. Elvevold, K., Kyrrestad, I., and Smedsrød, B. (2022). Protocol for Isolation and Culture of Mouse Hepatocytes (HCs), Kupffer Cells (KCs), and Liver Sinusoidal Endothelial Cells (LSECs) in Analyses of Hepatic Drug Distribution. Methods Mol. Biol. *2434*, 385–402. https://doi.org/10.1007/978-1-0716-2010-6_27.

STAR★METHODS

KEY RESOURCES TABLE

REAGENT or RESOURCE	SOURCE	IDENTIFIER
Antibodies		
Rabbit monoclonal anti-Fibronectin	Abcam	Cat# ab199056; RRID: AB_2802127
Rabbit polyclonal anti-Laminin	Abcam	Cat#ab11575; RRID: AB_298179
Rabbit monoclonal anti-CD11b	Abcam	Cat# ab133357; RRID: AB_2650514
Rabbit monoclonal anti-CD41	Abcam	Cat# ab134131; RRID: AB_2732852
Mouse monoclonal anti-E-cadherin	BD Biosciences	Cat# 610181, RRID: AB_397580
Rabbit monoclonal anti-F4/80	Cell Signaling Technology	Cat# 70076, RRID: AB_2799771
Rabbit polyclonal anti-α-SMA	Abcam	Cat# ab5694, RRID: AB_2223021
Rabbit polyclonal anti-VEGFA	Proteintech	Cat# 19003-1-AP; RRID: AB_2212657
Mouse monoclonal Anti-VEGFA	Abcam	Cat# ab1316; RRID: AB_299738
Rabbit polyclonal anti-Src	Cell Signaling Technology	Cat# 2123; RRID: AB_2106047
Rabbit monoclonal anti-p-Src	Cell Signaling Technology	Cat# 6943, RRID: AB_10013641
Rabbit polyclonal anti-YAP	Cell Signaling Technology	Cat# 17074, RRID: AB_2650491
Rabbit monoclonal anti-p-YAP	Cell Signaling Technology	Cat# 13008, RRID: AB_2650553
Rabbit polyclonal anti-p-MLC	Cell Signaling Technology	Cat# 3671; RRID: AB_330248
Rabbit polyclonal anti-MLC	Proteintech	Cat#10906-1-AP, RRID: AB_2147453
Rabbit polyclonal anti-CD14	Proteintech	Cat#17000-1-AP, RRID: AB_2919143
Mouse Anti-RhoA-GTP Monoclonal Antibody	NewEast Biosciences	Cat# 26904, RRID: AB_1961799
Rabbit polyclonal anti-RhoA	NewEast Biosciences	Cat# 21017, RRID: AB_2828037
Rabbit monoclonal anti-His-tag	Beyotime	Cat# AG8061, RRID: AB_3083011
Rabbit monoclonal anti-Flag-tag	Beyotime	Cat# AG8050, RRID: AB_2940884
Rabbit polyclonal anti-GAPDH	Proteintech	Cat#10494-1-AP, RRID: AB_2263076
Chemicals, peptides, and recombinant proteins		
RNAscope® 2.5 HD Reagent Kit-RED	ACD	Cat# 322350
RNAscope® 2.5 VS Probe- Mm-Adamts18	ACD	Cat# 452259
MolPure® Cell/Tissue Total RNA Kit	YEASEN	Cat# 19221ES50
Hifair® II 1st Strand cDNA Synthesis SuperMix for qPCR	YEASEN	Cat# 11123ES60
Hieff® qPCR SYBR® Green Mix	YEASEN	Cat# 11201ES08
FITC-Dextran 2000	TdB Labs	Cat# FD2000
Lipo8000™	Beyotime	Cat# C0533
DAPI	Beyotime	Cat# C1005
Critical commercial assays		
Modified Oil Red O Staining Kit	Beyotime	Cat# C0158S
Total Superoxide Dismutase Assay Kit with WST-8	Beyotime	Cat# S0101S
Hematoxylin-Eosin/HE Staining Kit	Solarbio	Cat# G1120
Modified Masson's Trichrome Stain Kit	Solarbio	Cat# G1346
Periodic Acid Schiff (PAS) Stain Kit, with Hematoxylin	Solarbio	Cat# G1281
Lipid peroxidation assay kit	Nanjing Jiancheng Bioengineering Institute	Cat# A106-1-2
MiniMACS Starting Kit	Miltenyi	Cat# 130-090-312
MACS CD146 (LSEC) MicroBreads, mouse	Miltenyi	Cat# 130-092-007
Flag-tagged protein immunoprecipitation kit	Beyotime	Cat# P2202S

(*Continued on next page*)

Continued

REAGENT or RESOURCE	SOURCE	IDENTIFIER
RhoA activity assay kit	NewEast Biosciences	Cat# 80601
Experimental models: Cell lines		
HEK 293T	Cell bank of the Chinese academy of sciences	N/A
Experimental models: Organisms/strains		
C57BL/6/129Sv mouse strain	Lu et al., 2017[70]	N/A
C.B17-scid immunodeficient mice	Shanghai Jihui experimental animal feeding Co., LTD	N/A
Carbon tetrachloride (CCl4)-induced liver fibrosis model	This paper	N/A
Diethylnitrosamine (DEN)-induced HCC model	This paper	N/A
Oligonucleotides		
Primers for Figures 1 and 5, see Table S1	This paper	N/A
Recombinant DNA		
pcDNA3.1(+)-*Adamts18* plasmid	This paper	N/A
pcDNA3.1(+)-*Fn1*-N81-290aa plasmid	This paper	N/A
pCMV6-*Adamts18* plasmid	Lu et al., 2020[25]	N/A
Software and algorithms		
Graphpad Prism	Graphpad software	https://www.graphpad.com/
Image J	NIH	https://imagej.net/

RESOURCE AVAILABILITY

Lead contact

Further information and requests for resources and reagents should be directed to and will be fulfilled by the lead contact, Dr. Wei Zhang (wzhang@sat.ecnu.edu.cn).

Materials availability

This study did not generate new unique reagents.

Data and code availability

- Data reported in this paper will be shared by the lead contact upon request.
- This paper does not report original code.
- Any additional information required to reanalyze the data reported in this paper is available from the lead contact upon request.

EXPERIMENTAL MODEL AND STUDY PARTICIPANT DETAILS

Animals

Adamts18 knockout mice with C57BL/6/129Sv strain were generated and genotyped as previously described.[70] The animals were housed in a specific pathogen-free facility under a 12-h light/dark schedule, with lights on at 07:00. Male and female mice were randomly used in this study unless otherwise stated. All animal experiments were approved by the Institutional Animal Care and Use Committee of East China Normal University (ECNU).

Carbon tetrachloride (CCl4) induced liver fibrosis model

8-week-old male *Adamts18*$^{+/+}$ and *Adamts18*$^{-/-}$ mice were used for CCl4-induced liver fibrosis experiment. Specifically, mice were injected intraperitoneally with CCl4 (dissolved in corn oil in a 1:4 ratio) at 1 μL/g body weight twice a week for four weeks. The mice were sacrificed 96 h after the last injection for pathological analysis.

Diethylnitrosamine (DEN) induced hepatocellular carcinoma (HCC) model

2-week-old male *Adamts18*$^{+/+}$ and *Adamts18*$^{-/-}$ mice were used for DEN-induced HCC experiment. Mice were injected intraperitoneally with DEN (25 mg/mL) at 10 μL/g body weight. The mice were then given a high-fat diet at 5 weeks of age and uniformly sacrificed at 9 months of age.

METHOD DETAILS

Materials

All reagents were purchased from Sigma–Aldrich (St. Louis, MO, USA) unless otherwise indicated. Primers for quantitative real-time RT-PCR (qRT-PCR) used in this study are listed in Table S1.

The list of reagents used in this study can be found in the key resources table.

An overview figure of the aim and the experimental set up can be found in Figure S6.

RNA *in situ* hybridization, qRT-PCR, Histology, immunohistochemistry, and immunofluorescence

RNA *in situ* hybridization (ISH) was performed following established protocols.[25] In briefly, fresh 5-μm-thick sections were used for ISH using the RNAscope 2.5 HDReagent Kit-RED (Advanced Cell Diagnostics, Hayward, CA). qRT-PCR was carried out using Hifair® II 1st Strand cDNA Synthesis SuperMix for qPCR and Hieff® qPCR SYBR® Green Mix. Total RNA was extracted from liver tissue using the MolPure® Cell/Tissue Total RNA Kit. The relative quantity of target mRNA was determined using the ΔΔCt method, with *Gapdh* serving as the reference gene. All reactions were performed in triplicate. For histology, liver tissues were fixed in 10% neutral buffered formalin for 24 h at room temperature (RT) and embedded in paraffin or OCT. Subsequently, paraffin sections were deparaffinized and hydrated. Liver sections were stained with hematoxylin and eosin (H&E), periodic acid and Schiff reagent (PAS), Oil Red O staining, or performed immunohistochemistry (IHC) and immunofluorescence (IF). Images of stained sections were captured randomly with light microscope (DMI3000, Leica, Wetzlar, Germany) and confocal microscope (SP8, Leica, Wetzlar, Germany).

Blood vessel cast

Casting agents were prepared as following steps. First, appropriate amount of ethylene perchloride resin (13%) dibutyl phthalate (2.7%), diamond glue (20%) and paint (5 g/100 mL) were added to the ethyl acetate solution and mixed evenly. Then, the mice were sacrificed and the chest was opened to expose the liver. The liver was flipped upward with a cotton swab containing PBS to expose the dorsal side of the liver, as well as the extrahepatic portal vein and inferior vena cava veins, and 4% sodium citrate saline was injected. A small incision was made in the inferior vena cava to drain the blood, after outflow of clear fluid from the opening, ethyl acetate and casting agent was pumped into the portal vein at a constant rate (All injected fluids need to be preheated to 37°C in advance). The liver was gently massaged with a wet cotton swab to promote uniform filling until the casting agent filled the tissue. The left outer lobe of the liver was removed and placed in PBS, left for an hour to allow the casting agent to fully cure, and then immersed in 15% KOH to corrode excess tissue. After standing at room temperature for 24 to 48 h, imaged with a body type dissecting scope (MZ61, Mshot, Guangzhou, China) after washed by running tap water.

Electron microscopy

For transmission electron microscopy (TEM), mice were sacrificed and perfused with normal saline solution. Mouse livers were fixed by perfusion 2.5% glutaraldehyde. We selected the left lateral lobe of the liver and took three tissue blocks (1*1*1 mm^3) from the central region. The blocks were fixed in 2.5% glutaraldehyde, followed by fixation with 1% osmium tetroxide. Dehydration was carried out by successive ethanol incubation, followed by embedding in plastic, ultrathin sectioning, and electron staining with lead citrate. Images were captured randomly with a transmission electron microscope (H-7650, Hitachi, Tokyo, Japan). The magnification of the image was 15000 times. For scanning electron microscopy (SEM), the steps for obtaining the samples were the same as those for the TEM samples. The tissue block size was about 3*3*3 mm^3, which were dehydrated in a graded ethanol series, critical-point dried, sputter-coated and examined using the scanning electron microscope (Gemini SEM 300, Zeiss, Oberkochen, Germany). The magnification of the image was 7000 times. Each liver section was analyzed for 3 fields, and three biological replicates were performed.

Multiphoton laser scanning confocal intravital microscopy (IVM)

Mice were anesthetized by intraperitoneal injection of Avertin according to their body weight (20 μL/g) and FITC-Dextran 2000 were injected into the caudal vein. Then, livers were exposed and the left lateral lobes were fixed on glass coverslips with dust-free paper soaked in PBS. Images of the exposed left lateral lobes were captured 15 min later using a multiphoton imaging system (FVMPE-RS, Olympus, Tokyo, Japan).

Enzyme linked immunosorbent assay

Enzyme linked immunosorbent assay (ELISA) was performed according to the manufacturer's instructions. The superoxide dismutase (SOD) and lipid hydroperoxide (LPO) values were measured by colorimetry, and then converted into SOD activity and LPO content in liver tissue.

Assay of liver vascular permeability

In this experiment, 2-week-old *Adamts18*$^{+/+}$ and *Adamts18*$^{-/-}$ mice were used to assess liver blood vessel permeability using Evans Blue dye as previously described.[71] Evans blue is a diazo salt fluorescent dye with high affinity (10:1) for albumin (the most abundant protein in plasma) and presents red fluorescence under the excitation of 550 nm. Specifically, 0.5% sterile solution of Evans blue in PBS without any particulate matter was slowly injected through the tail vein of the mouse (4 μL/g). Evans blue dye was allowed to circulate for 30 min. Animals were then perfused transcardially with PBS until fluid from the right atrium became colorless. All the mice were sacrificed at the same time, as fast as

possible. The livers were harvested immediately, and were sliced into 5-μm-thick sections using a cryostat. The level of liver vascular permeability can be assessed by simple visualization of the liver section under the excitation of 550 nm by a fluorescence microscope.

LSECs isolation

The primary LSECs were isolated from 2-week-old *Adamts18*$^{+/+}$ and *Adamts18*$^{-/-}$ mice. Briefly, liver was initially perfused with PBS and then with type IV collagenase solution preheated at 37°C. After perfusion, the liver was transferred to type IV collagenase solution, chopped to chyme and digested at 37°C for 8–10 min. The cell suspension was then filtered by a 70 μm screen and centrifuged at 50× *g* room temperature for 2 min. The supernatant rich in non-parenchymal cells was collected and centrifuged again. After centrifugation, the supernatant was centrifuged at 300× *g* for 10 min at 4°C. Cell precipitates were re-suspended with MACS buffer and purified using LSEC-specific CD146-based isolation on magnetic MicroBeads (MACS, MiltenyiBiotec, Germany) as previously described.[72,73] Freshly isolated primary LSECs were lysed to extract proteins for western blotting, or seeded on cell slides, cultured in Mouse LSEC Complete Medium (Precell, Wuhan, China), and immobilized for cell immunofluorescence after overnight culture.

Cell immunofluorescence

LSECs were fixed for 15 min with 4% paraformaldehyde at room temperature (RT) or for 10 min with pre-cooled anhydrous methanol at −20°C. Subsequently, the cells were cleaned with PBS and permeated with 0.2% Triton X-100 (this step is omitted for detecting membrane proteins). Cells were enclosed with 5% BSA at RT for 1 h. The cells were incubated with anti-CD14, anti-RhoA-GTP, anti-pMLC, and anti-pYAP antibodies overnight at 4°C, followed by incubation with the secondary antibody. Cells were counterstained with DAPI and imaged with Leica SP8 confocol microscope (Leica Microsystems, Wetzlar, Germany).

RhoA activity

RhoA activity assay was performed using RhoA activity assay kit as previously described.[37] Briefly, freshly isolated primary LSECs were lysed in lysis buffer. After determination of protein concentration by BCA method, the lysate containing the same amount of protein was diluted to 1 mL with lysis buffer, then incubated with anti-RhoA-GTP mouse monoclonal antibody for 2 h at 4°C. Subsequently, the solution was incubated with protein A/G agarose beads for 2 h at 4°C with shaking. After centrifugation, the beads were washed with lysis buffer, and eluted with SDS buffer. Proteins eluted from agarose beads were separated by SDS-PAGE and analyzed by Western blotting.

Cell culture and co-localization assay

HEK 293T cells stably transfected with pCMV6-*Adamts18* and empty vector and were cultured in DMEM supplemented with 10% FBS and antibiotics. After trypsin digestion, cells were counted and approximately 5 × 10^6 cells were injected subcutaneously into each 6-week-old male C.B17-SCID mice to form subcutaneous tumors. The mice were euthanized and the subcutaneous tumors were removed and used for ADAMTS18 and FN or FN and VEGFA immunofluorescence co-localization assay.

Protein–protein docking study

Homo sapiens ADAMTS18 protein prediction was downloaded from the AlphaFold protein structure database and used as receptor. Homo sapiens protein fragments of FN were found in the protein databank (PDB), and 13 of them were selected based on crystal resolution <2.00 Å. The ADAMTS18 structure was used as receptor, and protein fragments of FN were submitted as ligands to the GRAMM-X and analyzed by PDBePISA for docking analysis.

Co-immunoprecipitation (IP)

Flag-tagged protein immunoprecipitation kit was used to perform the experiment. HEK 293T cells were transiently single transferred and co-transfected with pCDNA3.1-*Adamts18* and pcDNA3.1-recombinant FN N-terminal protein (FN-N81-290 aa) by using Lipo8000. After 48 h of cell culture, lysates were added for protein extraction. Proteins were incubated with anti-DDK agarose overnight at 4°C and eluted with 3 × Flag polypeptide eluent. Proteins eluted from agarose beads were separated by SDS-PAGE and analyzed by Western blotting. Mouse IgG agarose gel and anti-Flag agarose gel were used for immunoprecipitation. Anti-Flag and anti-His antibody recognizing Flag-ADAMTS18, His-FN were used for immunoblotting.

QUANTIFICATION AND STATISTICAL ANALYSIS

Data were analyzed by Student's t test using the software package Prism version 8 (GraphPad, La Jolla, CA, USA). Data are shown as mean ± SD. A *p* value <0.05 was considered statistically significant. The statistical details of experiments can be found in the figure legends.